The embedded-atom method: a review of theory and applications

Murray S. Daw [a], Stephen M. Foiles [a] and Michael I. Baskes [b]

[a] *Theory Department, Sandia National Laboratories, Livermore, CA 94551-0969, USA*
[b] *Materials and Process Research Department, Sandia National Laboratories, Livermore, CA 94551-0969, USA*

Received 1 June 1992; in final form 4 September 1992

1993
NORTH-HOLLAND
AMSTERDAM–LONDON
NEW YORK–TOKYO

Contents

Materials Science Reports 9 (1993) 251–310
North-Holland

MATERIALS SCIENCE REPORTS

The embedded-atom method: a review of theory and applications

Murray S. Daw [a], Stephen M. Foiles [a] and Michael I. Baskes [b]

[a] *Theory Department, Sandia National Laboratories, Livermore, CA 94551-0969, USA*
[b] *Materials and Process Research Department, Sandia National Laboratories, Livermore, CA 94551-0969, USA*

Received 1 June 1992; in final form 4 September 1992

The embedded-atom method (EAM) is a semi-empirical, many-atom potential for computing the total energy of a metallic system. It is especially useful for systems with large unit cells, and is appropriate for metals with empty or filled d bands. With the EAM, the materials community has investigated many problems of interest: point defects, melting, alloying, grain boundary structure and energy, dislocations, segregation, fracture, surface structure, and epitaxial growth. In general, most of the EAM calculations have been carried out in close connection with experimental work. We review here the history, development, and application of the EAM.

1. Introduction

It is an appealing notion to consider the physical properties of materials on the fundamental scale of the atomic structure. Our knowledge of the atomic structure of solids has advanced considerably in recent years. It is now possible for experiments to resolve the atomic-scale structure of complex systems like interfaces, surfaces, and grain boundaries. These experimental breakthroughs have provided strong motivation for further theoretical investigations of structure. First-principles calculations are capable of explaining certain basic properties. In many cases, however, the complexity of the system demands more approximate methods. A simpler approach, which has been around for many years, is the pair potential. However, the pair-potential scheme omits a crucial piece of the physics of metallic bonding, and so falls short as a reliable tool. The past decade saw the development of the embedded-atom method (EAM) [1–5], which incorporated an approximation to the many-atom interactions neglected by the pair-potential scheme. The advent of the EAM allowed simulation of a very large set of interesting problems. This review emphasizes the physical insight that motivated the EAM, and summarizes some of the calculations of atomic-scale structure in metals that the EAM made possible.

Most of our questions regarding structure and thermodynamics can be answered from a knowledge of the total energy. The total energy of a solid at any atomic arrangement can be calculated, at least in principle, by solving the many-electron Schrödinger equation. This problem is overwhelming in practice. Some approximations to this scheme, such as the local-density approximation, reduce the complexity of the problem while hopefully retaining the important physics. However, even with recent impressive advances in computers and algorithms, these traditional band-structure calculations are impractical for systems with very low symmetry, such as grain boundaries.

At the other extreme, it has been useful to *assume* that the total energy of a solid, E_{coh}, takes the form of a sum over pair bonds:

$$E_{\mathrm{coh}} = \tfrac{1}{2} \sum_{i,j(j\neq i)} V(R_{ij}). \tag{1}$$

In this picture, the bonds between atoms are independent of each other (that is, the strength of one bond is unaffected by the presence of other bonds). This ansatz is very simple and very useful for the problems at hand. However, there is a major difficulty with this approach. It is *not* possible to show theoretically that the total energy can be expressed in the form of pair bonds (eq. (1)). The error in the pair-potential approximation arises from the fact that, in general, the bonds between atoms are not independent of each other.

One can see this effect by considering the cohesive energy of a series of crystal structures that differ only by the coordination, Z, of a typical atom. It is easy to see from the pair model that the cohesive energy scales linearly with Z, so that $E_{\mathrm{coh}} \propto -Z$. But the reality is that the cohesive energy scales more weakly. On rather general grounds [6], one can estimate that the energy should scale something like $-Z^{1/2}$. This is like saying that the strength of an additional bond is not constant but rather decreases with increasing Z.

Coordination-dependent, or many-atom, interactions manifest themselves in the fundamental properties of solids. One can illustrate this point nicely by examining the elastic constants, vacancy formation energy, cohesive energy, and melting points, in table 1. In a cubic solid held together purely by pairwise, central-force interactions, it is simple to demonstrate that two distinct elastic constants are equal. That is, $C_{12} = C_{44}$, which is known

Table 1
Some indicators of many-body effects in some fcc metals. Ni, Cu, Pd, Ag, Pt, and Au are compared with a Lennard-Jones solid (LJ) [7,8], taken as a typical two-body system, and two rare-gas solids. This table was inspired by and partially copied from Ercolessi et al. [9]

Solid	$\frac{C_{12}}{C_{44}}$	$\frac{E_v^f}{E_{coh}}$	$\frac{E_{coh}}{kT_m}$
pair potential			
LJ	1.0	1.00	13
rare gases			
Ar	1.1	0.95	11
Kr	1.0	0.66	12
fcc metals			
Ni	1.2	0.31	30
Cu	1.6	0.37	30
Pd	2.5	0.36	25
Ag	2.0	0.39	27
Pt	3.3	0.26	33
Au	3.7	0.23	34

as the "Cauchy relation". A solid described by any central-force pair interaction, such as the Lennard-Jones pair potential, has the ideal ratio of $C_{12}:C_{44}$ of 1. So do the rare gases, which are the prototype Lennard-Jones systems. However, fcc metals generally have $C_{12}:C_{44}$ closer to 2. Some metals, like Au and Pt, have high values of $C_{12}:C_{44}$, between 3 and 4. These simple phenomenological observations reveal the presence of significant many-atom interactions. A similar statement can be made about the ratio of the vacancy formation energy (E_v^f) to cohesive energy (E_{coh}). In a purely pairwise solid, counting the broken pair-bonds shows that $E_v^f : E_{coh}$ is unity. A quick review of the metals shows that the fcc metals have values of this ratio closer to 0.35. Once again, Pt and Au appear to be unusual in their deviation from pairwise bonding. Another indicator is the ratio of the cohesive energy to the melting point. The fcc metals stand out as being distinctly non-pairwise. From arguments such as these, we have evidence that metallic bonding is distinctly non-pairwise and that deviation is stronger for Pt and Au than for Ni, Cu, Pd, or Ag.

The thesis of this review is that many of the interesting problems in the structure of metals require a treatment of the coordination-dependent bonding. It seems fruitful to look for a practical method that can be applied to low-symmetry systems and yet retains the many-atom aspects of bonding. Such an approach would be useful as a guide to exploring the essential physics, and as a tool for probing ahead of more accurate and expensive calculations.

It was with this in mind that Daw and Baskes [1,2] proposed the embedded-atom method. In this approach, we view the energy of the metal as the energy obtained by embedding an atom into the local electron density provided by the remaining atoms of the system. In addition, there is an electrostatic interaction. The ansatz they used is

$$E_{coh} = \sum_i G_i\left(\sum_{j\neq i} \rho_j^a(R_{ij})\right) + \tfrac{1}{2}\sum_{i,j(j\neq i)} U_{ij}(R_{ij}), \tag{2}$$

where G is the embedding energy, ρ^a is the spherically averaged atomic electron density, and U is an electrostatic, two-atom interaction. We define the embedding energy as the interac-

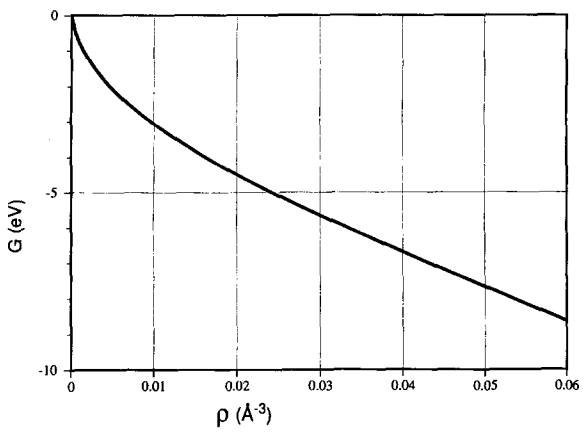

Fig. 1. Embedding energy for Ni as a function of the background electron density.

tion of the atom with the background electron gas. Fig. 1 illustrates a typical embedding energy. The background density for each atom in eq. (2) is determined by evaluating at its nucleus the superposition of atomic-density tails from the other atoms. Fig. 2 illustrates the electrostatic pair interaction.

A particularly appealing aspect of the EAM is its physical picture of metallic bonding. Each atom is embedded in a host electron gas created by its neighboring atoms. The atom–host interaction is described in a way that is inherently more complex than the simple pair-bond model. In this way, the embedding function incorporates some important many-atom interactions. It is possible to describe and understand interatomic interactions at defects in terms of either the embedding function or the effective many-atom interactions that arise from it. In particular, it is simple to demonstrate how bonding is affected by coordination. This naturally leads to an understanding of the difference between bulk and surface bonds, for example.

The EAM is currently the method of choice for doing semi-empirical calculations in close-packed metals; it combines the computational simplicity needed for larger systems with

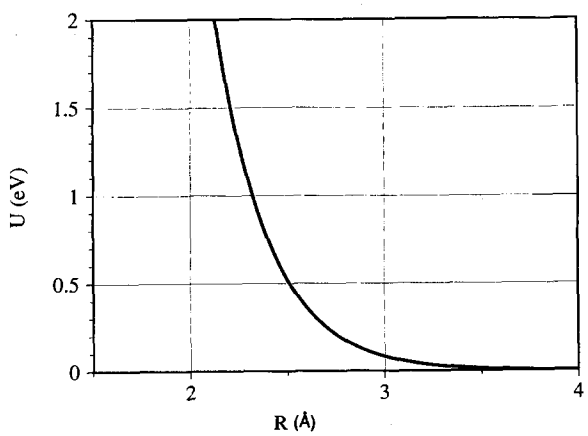

Fig. 2. Pair interaction for Ni as a function of separation.

a physical picture that includes many-atom effects and avoids some of the problems of the pair-potential scheme. This method has been applied successfully to bulk and interface problems, such as phonons [10], thermodynamic functions and melting point [11,12], liquid metals [13], defects [2–4], grain boundary structure [14–19], alloys [3,4,20,21], segregation to grain boundaries [21–23], interdiffusion in alloys [24,25], and fracture and mechanical properties [26–32]. The EAM has been applied to problems in surface structure [2–4,33–36], adsorbate phase diagrams [37–41], segregation to surfaces [42–48], surface structural order–disorder transitions [34], surface ordered alloys [35,47], surface phonons [49,50], and clusters on surfaces [51,52].

This review will discuss the history, development, and application of the EAM to a wide variety of problems in the physics of metals. We will review the fundamentals as well as the phenomenology of the approach, and go on to describe some of the numerous applications. We will focus on two types of applications: simple tests of the EAM, and more complicated problems that probably could not have been treated any other way.

This review devotes special attention to the work performed by the present authors, although several other groups have applied the EAM (or methods mathematically equivalent to the EAM). Though some of the work by other groups will be discussed at appropriate places in this review, we do not intend here to give a thorough review of the work by other groups, simply because that task long ago became impractical. (We apologize to those whose work has been omitted.) Certain remarks, however, about the general trends predicted by the EAM will pertain to the work by other groups as well.

There has been a great deal of work using methods related in spirit to the EAM. We include here only a partial list. The effective-medium theory [53–56] has been applied to a number of problems at the surface and in the bulk [57–62]. DePristo and co-workers have developed the corrected effective-medium theory [63–69]. The excellent review by Raeker and DePristo [67], makes a detailed comparison between the several variant theories in the family; this review will not cover this ground.

The relationships of various models of interatomic potentials and the concepts of pair and cluster functionals (the EAM is a pair-functional method) are discussed in the elegant review by Carlsson [70]; the reader is referred to that review for a larger view of work on interatomic potentials.

This review is organized as follows. Section 2 describes the development of the embedded-atom method and the interpretation in terms of many-atom interactions. In particular, we consider the effects of coordination on metallic bonding. Sections 3–8 give an overview of calculations we have done with the EAM, covering bulk properties, grain boundaries, surfaces, alloys, and mechanical properties. Finally, in section 9, we make a short summary and briefly explore possible avenues for future work.

2. Embedded-atom method

Some years ago, Friedel [71] suggested that the dissolution of hydrogen in copper was related to the dissolution of hydrogen in jellium (electron gas with a uniform, neutralizing positive background). He was led to the investigation of the Friedel oscillations, i.e. impurity-induced oscillations in the jellium density. More recently, detailed calculations of the impurity-in-jellium problem were carried out within the local-density approximation (LDA) by Puska, Nieminen, and Manninen [72]. The solutions give the self-consistent impurity-in-jellium charge density and the embedding energies as functions of the background gas density.

The impurity-in-jellium work formed the basis of the independent developments by Nørskov and Lang (effective medium [53]) and by Stott and Zaremba (quasiatom [73]). Nørskov and Lang showed in detail that the heat of solution of a light, interstitial impurity (e.g., H or He) in a host metal could be calculated by replacing the host with a suitable effective medium, which in this case was jellium. The heat of solution was then related to the embedding function, which is the energy associated with placing the impurity in jellium. Nørskov and his co-workers have had great success in calculating from first principles the heats of solution [54] and heats of chemisorption [74] of hydrogen in metals. The optimal density of the jellium was determined by weighing the background metallic electron density by the Hartree potential of the metal ion. Stott and Zaremba arrived at a similar idea, based on viewing the impurity as a quasiatom in a nearly uniform electron gas.

The basis of the EAM is the realization that the cohesive energy of a metallic system can be expressed in terms of embedding energies. Daw and Baskes [1,2] made this important generalization by proposing to view the cohesive energy of a metallic solid as composed of the embedding energy plus electrostatic interactions. In this view, each atom in the metal is embedded into the electron gas created by the other atoms. Atoms near a defect, such as a surface, are embedded into an electron gas of different density profile than atoms in the bulk. Daw and Baskes suggested the ansatz (2) that will be discussed here. They then obtained the functions empirically by fitting to properties of the bulk metals. The generality of the functions was tested by applying them to surfaces and other defects. This generalization allowed calculations of complex metallic structures to be done within the approximate embedding-energy framework. The EAM is thus a significant improvement in simplified total-energy calculations for metallic systems.

More recently, Jacobsen, Nørskov, and Puska [55], Manninen [75], and Kress and DePristo [63,64] re-examined the ansatz used in the EAM with arguments based on the effective-medium approach. Jacobsen et al. demonstrated how the cohesive energy of a metallic system could be related to the embedding energies, with corrections accounting for the d–d hybridization in the transition metals. Their approach showed that with the neglect of the d–d hybridization (valid for simple metals and presumably for early and late transition metals), the EAM expression is recovered. (For Al and Cu, for example, the practical application of the effective-medium theory is mathematically equivalent to the EAM.) The density of the effective medium was taken to be an unweighed average of the background density over the Wigner–Seitz cell of the atom. Kress and DePristo suggested using as a weighing function the electron density of the atom itself, so that the background density is related to the overlap of charge densities. Kress and DePristo, for their corrected effective-medium theory, added a correction for the inaccuracies in the definition of the optimal effective-medium density.

It is also possible to derive the EAM form from approximations made within density-functional theory [5]. This work will be summarized in section 2.1.

Several other methods, equivalent to the EAM in practice, have been proposed since the original work of Daw and Baskes. These methods all take the form of eq. (2), with differences due to specific parameterizations or functional forms and differences in the physical interpretation of the quantities. Finnis and Sinclair [76] proposed that the d–d hybridization could be approximated in the second moment, which is of the same form as eq. (2). Their "N-body" potential was intended to be applied to defects in bcc metals. The Finnis–Sinclair model is formally equivalent in the case of homonuclear metals to the EAM. For alloys, however, the Finnis–Sinclair model leads to a form different from the EAM. The "local-volume-forces" model represents an alternative parameterization of the EAM by Chen, Voter, and Srolovitz [77], and has been applied to surface relaxations and grain boundaries in binary metallic

alloys. The "glue" model of Ercolessi, Tosatti, and Parrinello [78,79] also belongs to the EAM class of models, and has been applied mainly to surface reconstructions. The "equivalent-crystal" model of Smith and Banerjea in its original implementation is mathematically equivalent to the EAM, though again the motivation is different [80,81].

2.1. Fundamentals

Our goal is to derive an approximate expression for the cohesive energy of a metallic system that is an explicit function of the positions of the atoms and which is simple to evaluate (i.e. eq. (2)). This derivation has been discussed in detail by Daw [5], and we will only summarize it here.

We start with the density-functional expression for the cohesive energy of a solid [82]:

$$E_{\mathrm{coh}} = G[\rho] + \frac{1}{2}{\sum_{i,j}}' \frac{Z_i Z_j}{R_{ij}} - \sum_i \int \frac{Z_i \rho(\boldsymbol{r})}{|\boldsymbol{r} - \boldsymbol{R}_i|}\, \mathrm{d}\boldsymbol{r} + \frac{1}{2}\int\int \frac{\rho(\boldsymbol{r}_1)\rho(\boldsymbol{r}_2)}{r_{12}}\, \mathrm{d}\boldsymbol{r}_1\, \mathrm{d}\boldsymbol{r}_2 - E_{\mathrm{atoms}}, \tag{3}$$

where the sums over i and j are over the nuclei of the solid, the primed sum indicates omission of the $i=j$ term, Z_i and $\boldsymbol{R}_i$ are the charge and position of the ith nucleus, the integrals are over $\boldsymbol{r}$ (or $\boldsymbol{r}_1$ and $\boldsymbol{r}_2$), and $r_{12} = |\boldsymbol{r}_1 - \boldsymbol{r}_2|$. E_{atoms} is the collective energy of the isolated atoms. $G[\rho]$ is the kinetic, exchange, and correlation energy functional.

We can go from eq. (3) to eq. (2) if we make the following two assumptions: (a) $G[\rho]$ can be described by $G[\rho] = \int g(\rho(\boldsymbol{r}), \nabla\rho(\boldsymbol{r}), \nabla^2\rho(\boldsymbol{r}), \ldots)\, \mathrm{d}\boldsymbol{r}$ where g is the density and is assumed to be a function of the local electron density and its lower derivatives; and (b) the electron density of the solid can be described as a linear superposition of the densities of the individual atoms $\rho_s(\boldsymbol{r}) \equiv \sum_i \rho_i^{\mathrm{a}}(\boldsymbol{r} - \boldsymbol{R}_i)$). The first approximation is motivated by studies of the response function of the nearly uniform electron gas. The second approximation is justified by the observation that, in many metals, the electron distribution in the solid is closely represented by a superposition of atomic densities. In addition, due to the variational nature of the energy functional, errors in the assumed density should only affect the energy to second order. It is also useful for us to define the embedding energy for an atom in an electron gas of some constant density $\bar{\rho}$ (neutralized by a positive background): $G_i(\bar{\rho}_i) \equiv G[\rho_i^{\mathrm{a}} + \bar{\rho}_i] - G[\rho_i^{\mathrm{a}}] - G[\bar{\rho}_i]$. Using these two assumptions and the definition for the embedding energy, we can obtain from eq. (3):

$$E_{\mathrm{coh}} = \sum_i G_i\Big(\sum_{j\neq i} \rho_j^{\mathrm{a}}(R_{ij})\Big) + \tfrac{1}{2}\sum_{i,j(j\neq 1)} U_{ij}(R_{ij}) + E_{\mathrm{err}}. \tag{4}$$

The error (E_{err}) is a function of the background density $\bar{\rho}_i$. Setting the error to zero gives an equation for the optimal background density.

The solution to $E_{\mathrm{err}} = 0$ is discussed in detail by Daw [5]. An approximation to the equation is provided by

$$\int_{\Omega_i} g(\rho_i^{\mathrm{a}} + \rho_{\mathrm{b},i})\, \mathrm{d}\boldsymbol{r} \approx \int_{\Omega_i} g(\rho_i^{\mathrm{a}} + \bar{\rho}_i)\, \mathrm{d}\boldsymbol{r}. \tag{5}$$

Here Ω_i is the volume around atom i. The background density for atom i, $\rho_{b,i}$, is the superposition of tails from neighboring atoms: $\rho_{b,i}(\boldsymbol{r}) = \sum_{j \neq i} \rho_j^a(\boldsymbol{r} - \boldsymbol{R}_j)$. This background should be slowly varying over most of Ω_i. In the limit that the background density is slowly varying compared to ρ_i^a, then the solution to eq. (5) is $\bar{\rho}_i = \rho_{b,i}(\boldsymbol{R}_i)$, which leads to the EAM form (eq. (2)).

Tests of these approximations and corrections to the EAM are discussed by Daw [5]. In particular, it is demonstrated that if the charge is allowed to redistribute, the EAM form can be recovered to lowest order in the charge relaxation. Large charge redistributions make the form inappropriate.

The many-atom interactions in the EAM originate with the embedding function. That is because the embedding function is non-linear for chemically active elements. This non-linearity reflects the saturation of the metallic bond by increasing the background density. Tracing the argument further, this saturation of the bond can be related to the Pauli exclusion principle. From this, one can see that the nature of the metallic bonding requires the embedding function to have positive curvature; that is, $G'' > 0$.

There are two caveats to become aware of at this point. First, the EAM will not work as well for systems where directional bonding is important, such as semiconductors and elements from the middle of the transition series. For more on this point, we encourage the interested reader to read the review by Carlsson [70]. That review describes the relationship of the EAM to concepts of bonding in transition metals, including the saturation of bonding in metallic systems. Second, any subtleties due to Fermi-surface or band-structure effects are ignored in the EAM, so that any situations where these are important should be treated carefully.

2.2. Phenomenology

Although the EAM form is calculationally convenient, it is often conceptually useful to visualize effective N-atom interactions. The two physical pictures (the first in terms of embedding energies, the second in terms of explicit N-atom interactions) are unified under the EAM. On one hand, the embedding picture (within the approximations made by the EAM) provides a compact scheme for computing energies. On the other hand, the N-atom interaction picture provides a more direct way to visualize interactions. The two pictures are equivalent in the EAM. One way to see this equivalence is to examine how the total energy changes when one makes small perturbations from a reference state.

We pick as a reference state a uniform solid. For this case, all the atoms have the same environment, so we define $\bar{\rho} = \sum_n \rho^a(\boldsymbol{R}_n)$ and $\overline{U} = \sum_n U(\boldsymbol{R}_n)$ where the sums are over the neighbors of a typical atom. Then the total energy of the uniform solid is $N[G(\bar{\rho}) + \frac{1}{2}\overline{U}]$, where N is the number of atoms.

If we now allow a small distortion of the lattice, each atom will experience a slightly different electron density, and the embedding energy can be expanded in the small difference. The cohesive energy of the solid can then be written as a sum of N-body interactions.

For small distortions, the change in the energy within the EAM is equivalent to the change in the sum of effective two- and three-atom interactions [13]:

$$\Psi_{ij}(\boldsymbol{R}) \equiv \tfrac{1}{2}\Big\{\Big[U_{ij}(\boldsymbol{R}) + 2G_i'(\bar{\rho}_i)\rho_j^a(\boldsymbol{R}) + G_i''(\bar{\rho}_i)\big(\rho_j^a(\boldsymbol{R})\big)^2\Big] + [(i \leftrightarrow j)]\Big\}, \tag{6a}$$

$$\chi_{ijk}(\boldsymbol{R}_i, \boldsymbol{R}_j, \boldsymbol{R}_k) \equiv G_i''(\bar{\rho}_i)\rho_j^a(R_{ij})\rho_k^a(R_{ik}) + (i \to j \to k \to i) + (i \to k \to j \to i). \tag{6b}$$

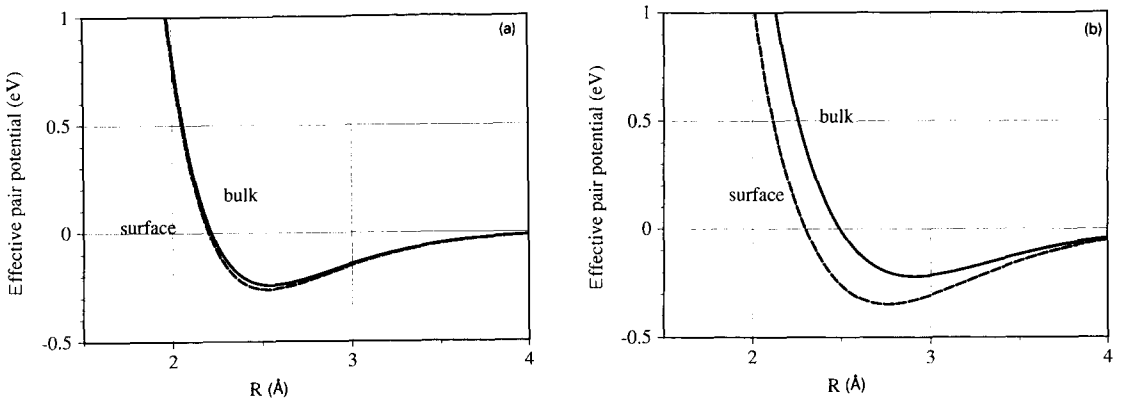

Fig. 3. (a) Effective pair interactions for Ni in two different environments: "bulk" and "surface". (b) Effective pair interactions for Pt in two different environments: "bulk" and "surface". (See text.)

Here the symbols involving arrows ($\rightarrow$) indicate a repetition of the previous expression with the indicated permutations of the indices. Higher-body interactions can be obtained by carrying the perturbation expansion to higher order. Note that the effective interactions depend only on the distances between the atoms and not (explicitly) on any angles. This is an important property of the EAM and is a direct result of the form of eq. (2).

The effective interactions in eqs. (6) are *environment dependent*, in that the interaction between two atoms depends on the slopes of their embedding functions, which depend on the $\bar{\rho}$ for each atom. As one goes to the surface, for example, the effective two-atom interaction becomes stronger and the bond length shortens. Within the EAM, this is a result of the requirement that $G'' > 0$. In this way, the EAM describes the effect of coordination on bond strength: the less-coordinated surface atoms tend to have stronger bonds and shorter bond lengths. This is the strength of the EAM, and is directly connected to the non-linearity of the embedding function. Note that if G is simply a linear function such that $G'' = 0$ in eqs. (6), then χ vanishes and the EAM can be replaced by a pair-potential model based on $\Psi(\boldsymbol{R})$. It is then straightforward to demonstrate that the properties of the solid will resemble those of "Lennard-Jonesium" of table 1. Thus the EAM contains pair potentials as a special case.

The *effective* pair interaction is illustrated in fig. 3, along with how the interaction changes with environment. Suppose we know the background density of a typical atom in the bulk, and for an adatom on the fcc(100) surface. If we plug these densities into eqs. (6), we can get a feel for the change in effective interactions due to the change in background densities. This is shown in fig. 3, where we have evaluated the background density of Ni and Pt in the bulk and for an adatom on the (100) surface. Here it is seen that, due to the curvature of the embedding function, the atoms on the surface tend to have stronger bonds and shorter bond lengths. It is also seen that the effect for Pt is stronger than for Ni. This is a manifestation of the observation made in section 1 that Pt and Au deviate furthest from simple pairwise behavior.

The trio interaction from eq. (6b) is positive and exponentially decaying; the trio interaction in the EAM is always repulsive. Notice that it is the sum of three terms, each of which depends only on two bond lengths and no angles. It is this lack of angular dependence that makes the EAM in its present form less applicable to metals from the center of the transition series.

2.3. Empiricism

The embedding function and pair interaction can be obtained from first principles, as was discussed in section 2.1 and described in detail by Daw [5] (also see Jacobsen et al. [55], for a different treatment). These first-principles functions do reasonably well in describing the properties of nickel. However, in practice, we have taken a semi-empirical approach, where the fundamental theory has guided the fitting of the embedding function and pair interaction to basic bulk properties. In general, we have fitted to lattice constant, cohesive energy, elastic constants, and vacancy formation energy. Notice that these are precisely the properties that clearly show the many-atom properties of the interactions in the solid (see table 1). We have also found it useful to require that the cohesive energy as a function of lattice constant follow the "universal binding curve" of Rose et al. [83]. This restriction appears to guarantee that the anharmonic properties are treated well. In other papers, we have also fitted to the dilute heats of alloying for binary alloys [3,4] or stacking fault energy [27]. In general, the fits are over-determined, and the fact that we can achieve a reasonable fit at all is in some sense a check of the EAM form. Functional forms have varied from case to case. In some cases, the functions are determined by general splines. In other cases, we have found it more useful to use analytic functions.

We include in table 2 a summary of the functions we have published. Because the functions are approximations, it is wise to understand the sensitivity of results to different parameterizations. For example, a study of Pd adatom diffusion on a Pd(100) surface could be performed both with functions from Daw and Baskes [2] and Foiles [13]. Also, the table emphasizes that EAM functions generally are not transferable: for example, functions determined separately for Ni and Pd likely will not treat the Ni–Pd alloy properly. The safest approach is to view the EAM as a means for interpolating between known quantities, or extrapolating only slightly away from known quantities.

A convenient starting point for fitting functions is the analytic work of Johnson [85,86].

When comparing the embedding functions and pair interactions from different sources, it is important to be aware of an ambiguity in the practical implementation of eq. (2). This results from the observation that adding a linear contribution to the embedding function can be exactly compensated for by a change in the pair interaction [48]. (This is related to the observation made above – that a linear embedding function, G, leads to a purely pairwise model.) For this reason, sets of embedding functions and pair interactions can appear to be

Table 2
A brief summary of functions determined by the present authors. All functions are determined semi-empirically except for those in Daw [5], which are calculated from first principles

Authors	Elements	Intended applications
Daw and Baskes [1,2]	Ni, Pd, H	elemental Ni, Pd H in solution and on surfaces of Ni, Pd
Foiles [13]	Cu, Ag, Au, Ni, Pd, Pt	elemental metals
Foiles [42]	Cu, Ni	Cu–Ni alloy system
Daw, Baskes, Bisson and Wolfer [27]	Ni, H	fracture, dislocations, H embrittlement
Foiles, Baskes and Daw [3,4]	Cu, Ag, Au, Ni, Pd, Pt	dilute alloys
Foiles and Daw [84]	Ni, Al	Ni-rich end of Ni–Al alloy system
Daw [5]	Ni	elemental Ni
Hoagland, Daw, Foiles and Baskes [30]	Al	elemental Al

quite different and in fact be equivalent. In particular, the freedom to vary the linear part of the embedding function means that one can have pair interactions that are purely repulsive, purely attractive or of a Morse-like shape and the total energy, which is the physically relevant quantity, will be the same. A good way to compare potentials is to compare the effective pair and trio interactions defined in eqs. (6) since they are independent of this ambiguity.

3. Overview of applications

The EAM has been applied to a large variety of problems related to properties of metals. From the EAM we obtain information on the structure, dynamics, phase transitions, vibrations, diffusion, and segregation. Some of the applications of the EAM appearing in the literature are reviewed in the following. We consider the following general topics: bulk properties (section 4); grain boundaries (section 5); surfaces (section 6); alloys (section 7); and mechanical properties (section 8). In this review we concentrate on applications that are simple tests of the EAM or which highlight the many-atom nature of the EAM.

The EAM is typically implemented in one of four different types of calculations: (1) energy minimization, (2) molecular dynamics, (3) Monte Carlo, or (4) vibrational-normal-mode analysis. The current practical limitations of EAM calculations on a CRAY-XMP, for example, allow molecular-dynamics simulations of up to 35000 atoms. (One of the virtues of the EAM is that supercomputers are not essential. Smaller calculations can be performed easily using high-performance workstations.) Simulated times for molecular dynamics typically run up to tens of picoseconds. Generally, the calculational cost scales linearly with the number of atoms. Monte Carlo simulations based on the EAM are in practice capable of approximately 10^5 iterations per atom. These simulations are most useful for annealing structures and obtaining transition temperatures or equilibrium concentration profiles. The dynamical matrix can be obtained analytically and the vibrational normal modes obtained by matrix diagonalization. Normal-mode calculations are currently possible for unit cells of up to about 260 atoms.

In each section, we consider results that have been calculated with specified EAM parameterizations (see table 2). The details of results do depend on the specific parameterizations. In spite of that, we will usually not be very careful in this review to explain which specific functions were used for a given calculation. Rather, it is assumed that the interested reader will refer to the published papers which do have such details spelled out.

4. Bulk properties

First we consider the work on some bulk properties: (1) phonons; (2) liquids; (3) thermal expansion, melting, and thermodynamic functions; and (4) point defects.

To be a reliable tool, any model of energetics must give a reasonable representation of these simple properties. With this in mind, most of the calculations discussed in this section are intended to show that the EAM gives a reasonable description of metallic bonding.

4.1. Bulk phonons

The phonon spectrum is obtained from the force-constant tensor [87], $\mathbf{K}_{ij}$, which can be derived from eq. (2) in a straightforward way. The result is [50]

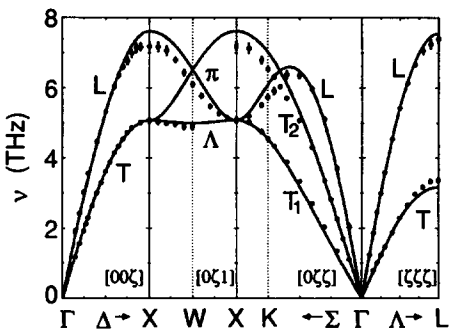

Fig. 4. Calculated and measured bulk phonon frequencies of fcc Cu. The experimental points, taken from Svensson et al. [88], are the solid circles with error bars. (From Nelson et al. [50].)

$$\mathbf{K}_{ij} \equiv \frac{\partial^2 E_{\text{tot}}}{\partial \boldsymbol{R}_i \, \partial \boldsymbol{R}_j} = -\mathbf{A}_{ij} + G_i''(\bar{\rho}_i)\rho_j^{a\prime}(R_{ij})\hat{\boldsymbol{r}}_{ji}\boldsymbol{g}_i + G_j''(\bar{\rho}_j)\rho_i^{a\prime}(R_{ij})\boldsymbol{g}_j\hat{\boldsymbol{r}}_{ij}$$

$$+ \sum_{k(\neq i,j)} G_k''(\bar{\rho}_k)\rho_j^{a\prime}(R_{jk})\rho_i^{a\prime}(R_{ik})\hat{\boldsymbol{r}}_{jk}\hat{\boldsymbol{r}}_{ik}, \tag{7a}$$

where

$$\mathbf{A}_{ij} = \Psi_{ij}''\hat{\boldsymbol{r}}_{ij}\hat{\boldsymbol{r}}_{ij} + (\Psi_{ij}'/R_{ij})(\mathbf{1} - \hat{\boldsymbol{r}}_{ij}\hat{\boldsymbol{r}}_{ij}),$$

$$\Psi_{ij} = G_i'(\bar{\rho}_i)\rho_j^{a}(R_{ij}) + G_j'(\bar{\rho}_j)\rho_i^{a}(R_{ij}) + U_{ij}(R_{ij}),$$

$$\boldsymbol{g}_i = \sum_j \rho_j^{a\prime}(R_{ij})\hat{\boldsymbol{r}}_{ij}. \tag{7b}$$

Here the unit vector $\hat{\boldsymbol{r}}_{ij} = (\boldsymbol{R}_i - \boldsymbol{R}_j)/R_{ij}$ and the primes denote differentiation with respect to the argument. The dynamical matrix for the system, which yields the squared phonon frequencies and polarizations, can be constructed from $\mathbf{K}_{ij}$.

The tensor $\mathbf{A}$ above represents the contribution to $\mathbf{K}$ from the environment-dependent, effective pair potential Ψ_{ij} (discussed in section 2.2). The other terms in $\mathbf{K}$ include explicit many-atom contributions, which depend on the environment through the quantities $\boldsymbol{g}$. Thus the phonons are directly related to the basic interactions in the solid.

The bulk phonons of fcc Ni, Pd, and Cu were calculated along several symmetry lines and compared to experiment [10,49,50]. Good agreement between theory and experiment is found, as is illustrated for the case of Cu in fig. 4. The agreement near the zone center is to be expected, because the functions are fitted to the elastic constants. However, agreement over the full zone was obtained as well, and this was not guaranteed by the fitting. Careful comparison over the full zone has been carried out by Luo et al. [89,90].

4.2. Liquids

Above the melting point, the static structure factors of various liquid transition metals were computed by Foiles [13]. The structure factors were obtained by averaging over molecular-dynamics simulations performed at elevated temperatures. The results for Ag are shown in fig.

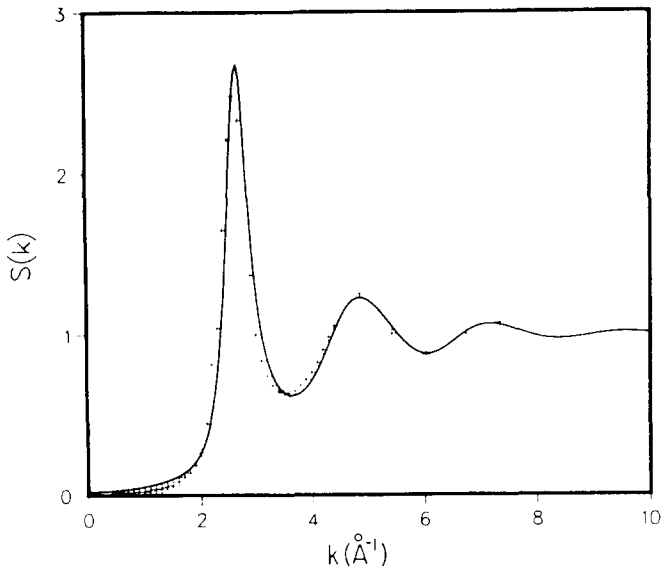

Fig. 5. Static structure factor $S(k)$ for liquid Ag at $T = 1270$ K and $n = 0.0517$ Å^{-3}. The solid line is the EAM result and the points are the experimental data from Waseda and Ohtani [91]. (From Foiles [13].)

5. The agreement between theory and experiment for the structure factors was quite good and was comparable to the agreement between different experimental determinations. The results also indicated that the equilibrium zero-pressure densities were within about 1 or 2% of the experimental values.

In the work on liquids, Foiles also presented a derivation of the effective pair interactions (section 2.2) and calculated the structure factors based on these effective pair interactions from the theory of liquids. The agreement between the MD simulations with the full EAM and the reference-hypernetted-chain-equation results with the effective pair potentials was quite good, reiterating the relationship between the EAM and the effective-interaction concept.

4.3. Thermal expansion, melting, and thermodynamic functions

Some of the thermodynamic properties predicted by the EAM have been computed for the metals Ni, Pd, Pt, Cu, Ag, and Au [11,12]. In particular, the thermal expansion, free energies as a function of temperature for both the liquid and solid states, and the melting point have been computed. These properties are interesting in part as a test of the interactions. In particular the thermal expansion is a test of the anharmonic part of the interactions. (Recall that totally harmonic interactions yield zero thermal expansion so the thermal expansion reflects the higher derivatives of the interactions.) The results for the melting point, aside from being an important test, are useful in simulation studies of the thermal behavior of these metals at high temperatures.

The determination of the thermodynamic functions over the whole temperature range and for both liquid and solid phases requires a variety of types of calculations. Monte Carlo simulations performed at constant pressure and temperature can be used to determine the density (lattice constant) and enthalpy of either the solid or liquid phase. It should be

recalled, though, that the Monte Carlo simulations evaluate the classical partition function and so do not include quantum-mechanical contributions to the thermodynamics such as zero-point motion and the freezing-out of modes at low temperatures. Thus the Monte Carlo simulations can only be used at temperatures comparable to or above the Debye temperatures for these materials. In addition, the simplest Monte Carlo techniques do not determine the free energy directly, only the enthalpy. If the free energy is known at some point, the enthalpy values can be used to determine the free energy at other temperatures by the thermodynamic expression:

$$\frac{\mathrm{d}}{\mathrm{d}T}\left(\frac{G}{T}\right)_{N,P} = -\frac{H}{T^2}. \tag{8}$$

For low-temperature solids, the free energy and thermodynamic functions can be computed using quasi-harmonic calculations [87]. These calculations correctly include the quantum-mechanical effects that are important at low temperatures and can be used to directly calculate all the thermodynamic functions including the free energy. This approach cannot be used at high temperatures because the amplitude of the thermal vibrations may be large enough that the harmonic approximation is no longer sufficiently accurate. Thus for the solid phase, the free energy can be computed at low temperatures using the quasi-harmonic approximation. At higher temperatures, the free energy can be determined using eq. (8), and the enthalpies determined from the Monte Carlo simulations.

For the liquid state, the free energy is needed at some temperature before eq. (8) can be used to extend it to all temperatures using enthalpies from isobaric Monte Carlo simulations. This can be done by performing Monte Carlo simulations at constant temperature, volume and chemical potential (i.e. in the grand canonical ensemble). The free energy is then just the chemical potential. The chemical potential is adjusted to produce zero pressure. In practice this procedure can only be performed at high temperatures (about twice the melting point) so that one can obtain reasonable statistics. Eq. (8) in conjunction with isobaric Monte Carlo simulations determines the free energy near the melting point.

The quasi-harmonic calculations were used to determine the linear coefficient of thermal expansion at room temperature [11]. This was motivated by the observation that the coefficient of thermal expansion predicted by the Finnis–Sinclair interactions for the bcc metals was very poor and in some cases negative [92]. The resulting values are presented in table 3 along with the experimental values. The agreement between the calculations and theory is generally quite good. The thermal expansion has also been computed over the entire

Table 3
Comparison of the linear coefficient of thermal expansion at room temperature computed using the EAM and experimental values [93] in units of 10^{-6}/K. From Foiles and Daw [11]

Element	α(EAM)	α(exp)
Cu	16.4	16.7
Ag	21.1	19.2
Au	12.9	14.1
Ni	14.1	12.7
Pd	10.9	11.5
Pt	7.8	8.95

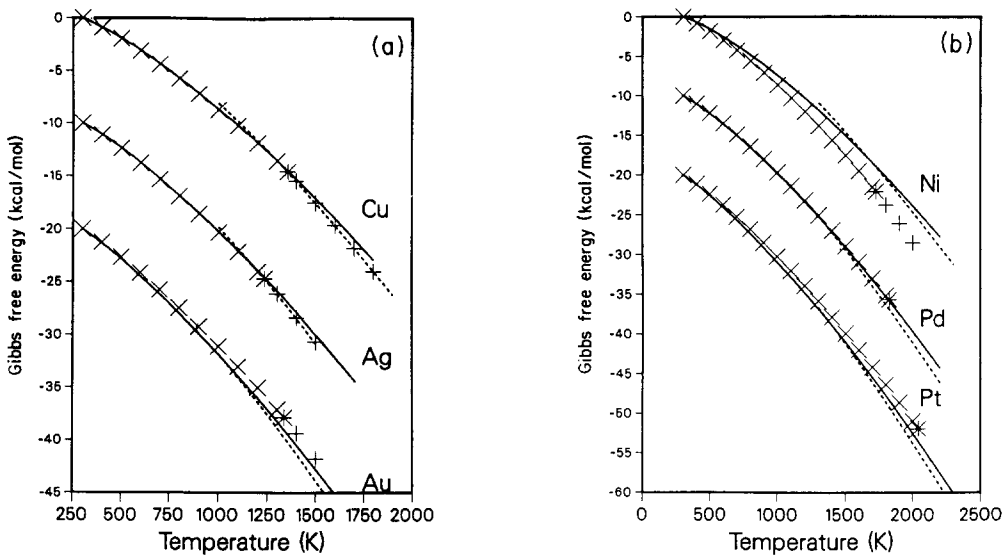

Fig. 6. Gibbs free energy of the solid and liquid phases of (a) Cu, Ag and Au and (b) Ni, Pd, and Pt in units of kcal/mol and referenced to the free energy at 300 K. The vertical axis applies to Ni and Cu with the other curves offset by 10 kcal/mol. The points represent the experimental values [94] (× for solid and + for liquid phase). The solid curves are the EAM solid free energies and the dashed curves are the EAM liquid free energies. (From Foiles and Adams [12].)

temperature range [12] and in all cases the results are reasonable with somewhat larger errors in the density at high temperatures than at room temperature.

The free energies of both the solid and liquid phases are presented in fig. 6. For the case of Cu and Ag, one sees that the agreement between the calculations and experiment is extremely good. For Au, Pd, and Pt the agreement is poorer but still reasonable. The agreement is worst for Ni. The intersection of the solid and liquid free energies determines the melting points. These are shown in table 4 along with the experimental values. The agreement is reasonable. Note that the agreement for Ni is very good. However, the free energy results for Ni were in poor agreement with experiment, suggesting that the good result for the melting point of Ni is fortuitous. In evaluating the degree of agreement between theory and experiment for the melting point, it is important to realize the sensitivity of the predicted melting point to errors in the free energies. The difference in the slopes of the solid and liquid free energies at the melting point is given by $\Delta H/T_m$, where ΔH is the latent heat of melting. For the elements

Table 4
Comparison of theoretical and experimental melting points (K). From Foiles and Adams [12]

Element	EAM	Exp.
Cu	1340	1358
Ag	1170	1234
Au	1090	1338
Ni	1740	1726
Pd	1390	1825
Pt	1480	2045

considered here this has a value of about 10^{-4} eV/atom K. This implies that an error of 0.01 eV in the free energy difference can lead to an error of 100 K in the melting point.

Noticing the entries in table 1, it is gratifying that we can obtain reasonable values for the ratio of cohesive energy to melting point for the fcc metals. The prediction of this ratio is particularly encouraging and implies that the model correctly accounts for anharmonic and many-atom interactions in both the liquid and solid phases.

4.4. Point defects

The EAM has been used to compute some of the basic properties of point defects in the fcc metals Cu, Ag, Au, Ni, Pd and Pt [3,95], and these are shown in table 5. These defect properties include vacancy formation and migration energies, divacancy binding energies and self-interstitial geometry, formation energy and migration energies. It should be recalled that the vacancy formation energies are used in the determination of the functions. (Recall that the ability to reproduce vacancy formation energy is one of the practical advantages of the EAM over strictly pair interaction models as discussed in section 1.) The binding energy of divacancies was computed to be 0.1 to 0.2 eV for these metals, which is in accord with the available experimental information. The structure of self-interstitials was also examined. In fcc metals, a self-interstitial atom pairs with a lattice atom to form a "dumbbell" with its center on a lattice site. The energies of dumbbells oriented along the [100], [110] and [111] directions were computed and the results show that the [100] orientation is preferred for all of these metals. The migration energy of the self-interstitials was also computed and found to be small (~ 0.1 eV) for all of these metals. Both of these results are consistent with the experimental observations of self-interstitial properties.

Adams, Foiles and Wolfer [24,25] have performed a detailed comparison of the vacancy self-diffusion and impurity diffusion predicted by the EAM and experiment. In this study, slightly modified versions of the functions developed by Foiles et al. [3] were used. In determining these new functions, more current experimental values of the vacancy formation

Table 5
Calculated point-defect properties: vacancy migration energy, E_v^m, vacancy formation volume, ΔV_v^f, divacancy binding energy, E_{2v}^b, divacancy migration energy, E_{2v}^m, self-interstitial formation energy, E_{si}^f, self-interstitial formation volume, ΔV_{si}^f, and self-interstitial migration energy, E_{si}^m. Ω is the equilibrium atomic volume. The upper values are the theoretical results and the lower values are experimental where available. All energies are in eV. From Foiles et al. [3,4] (see these papers for the references to the experimental work)

	Cu	Ag	Au	Ni	Pd	Pt
E_v^m	0.67	0.78	0.64	1.06	0.74	0.82
	0.71	0.66	0.83	1.3		1.43
$\Delta V_v^f/\Omega$	−0.27	−0.18	−0.41	−0.12	−0.39	−0.45
	−0.22	−0.06	−0.55			
E_{2v}^b	0.16	0.13	0.09	0.23	0.14	0.14
	0.12	0.38	0.2–0.6	0.33		0.1–0.2
E_{2v}^m	0.38	0.55	0.49	0.66	0.47	0.56
	0.71	0.57	0.70	0.83		1.1
E_{si}^f	3.30	3.26	2.46	4.52	3.05	3.24
$\Delta V_{si}^f/\Omega$	1.74	2.05	1.47	2.11	1.52	1.40
	1.45					
E_{si}^m	0.09	0.09	0.06	0.14	0.08	0.07
	0.12			0.14		0.063

Table 6
Comparison of the activation energies (in eV) for self-diffusion by a monovacancy mechanism. The "Exp." numbers were a composite of theoretical analyses based on several sets of experimental data (for more details, see Adams et al. [24])

Metal	EAM	"Exp."
Cu	2.02	2.07
Ag	1.74	1.78
Au	1.69	1.74
Ni	2.81	2.88
Pd	2.41	< 2.76
Pt	2.63	2.66

energies were used in the fitting process. The activation energy for vacancy self-diffusion in these metals was computed and found to be in excellent agreement with experiment. The comparison is shown in table 6. The activation energy for diffusion, Q, is the sum of the vacancy formation energy and the vacancy migration energy. Because the vacancy formation energies agree with experiment (by construction) and the activation energies, Q, also agree, one deduces that the vacancy migration energies computed using the EAM are reasonable.

Effective activation energies for the diffusion of substitutional impurities by a vacancy mechanism were also computed for all combinations of the above elements. The diffusion rates of substitutional impurities can be determined from the "five-frequency formula" as described in a review by LeClaire [96]. This expression relates the overall diffusion rate of the impurities to the rate of the five different types of vacancy jumps in the vicinity of a substitutional impurity. The activation energies of these various vacancy jumps were computed using the EAM. This allowed the impurity diffusion to be computed as a function of temperature and the results were fitted to an Arrhenius form. This yielded the effective activation energy for impurity diffusion. The computed activation energies are compared with experiment in table 7 for those combinations for which experimental data are available. The agreement is typically within 0.1 to 0.2 eV with the worst case being 0.3 eV. The agreement between experiment and theory is best for combinations of noble metals.

5. Grain boundaries

Numerous investigators have computed the atomic structure of grain boundaries using the EAM. In this paper we will briefly describe some of this work. The calculations will address a number of questions:

(1) How do the structures computed with the EAM compare with experimental determinations of the structure?
(2) Do the many-body effects present in the EAM make a significant contribution to the computed structure and properties?
(3) What are the elastic properties of grain boundaries?
(4) What are the effects of finite temperature on grain boundaries?

The structure of grain boundaries can be calculated by the usual energy-minimization techniques. There are some subtleties, though, that must be considered [14,15]. First, there are usually several metastable structures of the boundary that correspond to different relative translation of the two crystals. Because energy-minimization techniques only find local

Table 7
Comparison of theoretical and experimental values of the activation energies for impurity diffusion, Q, in eV. The experimental references are cited in Adams et al. [24]

System	EAM	Exp.
Ag in Cu	2.05	2.02
Au in Cu	1.88	1.98
Ni in Cu	2.37	2.46
Pd in Cu	2.06	2.36
Pt in Cu	2.20	2.42
Cu in Ag	1.92	2.00
Au in Ag	2.04	2.06
Pd in Ag	2.19	2.46
Pt in Ag	2.33	2.44
Ag in Au	1.80	1.75
Cu in Au	1.82	1.76
Ni in Au	1.90	1.95
Pt in Au	2.07	2.09
Pd in Au	1.93	2.02
Ag in Ni	2.68	2.89
Cu in Ni	2.76	2.64
Au in Pt	2.49	2.61
Ag in Pt	2.71	2.68

minima, several different initial translation states must be tested to find the lowest-energy configuration. In addition, it is sometimes possible to obtain lower-energy states by adding or removing atoms from the boundary. (This corresponds to the physical process of trapping self-interstitials and vacancies at the boundary.) Finally, it is possible that the period of the lowest-energy structure of the boundary may be larger than the minimum period required by the geometry of the two adjoining crystals. For example, in a study of $\Sigma 5(210)/[001]$ symmetric tilt boundary in Au, Foiles [14] found three different metastable structures that were very close in energy. The three structures had different periods along the tilt axis and were formed by removing atoms from the initial assumed structure. This example demonstrates that care must be taken when computing the structure of boundaries.

5.1. Structure

We have performed detailed comparisons between the computed atomic structures of grain boundaries and that obtained from experiment – either from high-resolution electron microscopy or from X-ray diffraction. A great deal of work has been done on both twist and tilt boundaries in Au and Al.

The structure of twist boundaries in Au has received a great deal of attention [15,97,98]. Fitzsimmons and Sass [97] experimentally determined the atomic positions at a $\Sigma 13[001]$ symmetric twist boundary by inverting X-ray diffraction intensities from the grain boundary. The resulting positions were compared with calculations using the EAM by Foiles [15] and it was found that the calculations and experiment were in very good agreement. The typical difference in the positions was 0.05 Å with the largest difference being 0.11 Å. This error is to be compared with the experimental uncertainty that was estimated to be about 0.06 Å by Fitzsimmons and Sass.

In addition to the atomic positions, the amplitudes of the atomic vibrations were extracted from the Monte Carlo simulations to compare with the assumptions made about the Debye–Waller factor in the experimental analysis. It was found that the vibrational amplitudes at the boundary are larger than in the bulk. Depending on the specific atomic environment and the direction of the vibration, the square of the amplitudes could be as much as a factor of 1.9 larger in the boundary than in the bulk. This result compares favorably with the experimental assumption of a factor of 1.5.

Majid et al. [98] have performed a joint experimental and theoretical study of a series of twist boundaries in Au. They computed the atomic structure using the EAM and from this structure computed the X-ray diffraction expected from the boundary. These diffraction intensities were then compared with experimental X-ray diffraction intensities. In all cases they found reasonable agreement between the computed and measured intensities – suggesting that the EAM provides a good description of the grain boundary structure.

Structure determination using high-resolution transmission electron microscopy (HRTEM) is less direct. In this case, one takes a candidate structure (such as a minimum-energy configuration produced by an EAM calculation) and simulates the image that one would see in the microscope. This simulated image is compared to the experimental image. Note that in the bulk and for certain microscope conditions, one sees bright spots which correspond to the atomic columns. At a boundary, though, intensity maxima can occur which do not correspond to a column of atoms, but rather to a channel. Without the detailed atomistic simulations, this bright spot might be misinterpreted as a column of atoms and an incorrect boundary structure might be deduced. These results also indicate the need to perform the atomistic simulations in conjunction with the image simulation to interpret the high-resolution microscopy.

As an example, consider the work done of the $\Sigma 9$ tilt boundary in Al. Experimentally, this boundary was observed in HRTEM [16,18] to be composed of atomically flat micro-facets. Two distinct, symmetric structures with $(2\bar{2}1)$ boundary planes were identified with individual micro-facets – one with glide-plane symmetry and the other with mirror-plane symmetry. The lowest-energy structures calculated using the EAM were found to be in excellent agreement with the observed micro-facet structures. The only relaxed configuration consistent with the mirror-plane symmetric structure was a reconstructed one in which the periodicity is doubled along the tilt axis. The micrograph of this structure is compared to the theoretical image in fig. 7.

Similarly, HRTEM images of the $\Sigma 99(557)$ $\langle 110 \rangle$ symmetric tilt have been compared [17] to the structure predicted by the EAM. The theoretical structure closely matches the experimental results.

The structures of several tilt boundaries in Au have been computed and compared to the results of HRTEM by Merkle [99] and by Cosandey et al. [100]. They find that the qualitative structure computed by the EAM is in good agreement with the observations but that the EAM typically underestimates the overall expansion of the boundary compared to the high-resolution electron microscopy results.

5.2. Role of many-body interactions

One point should be made about these various calculations of grain boundary structure using the EAM. It appears that in most cases very similar results are obtained using a pair-potential treatment of the energetics. Thus the many-body interactions inherent in the EAM do not appear to dominate these properties even though grain boundaries are a region

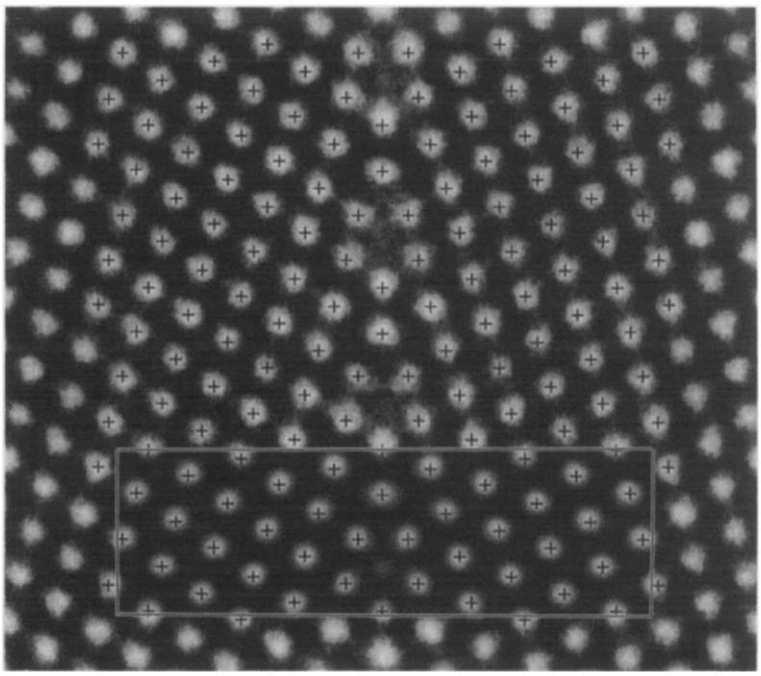

Fig. 7. Comparison of theory and experiment for a grain boundary in Al. The grain boundary is the $\Sigma 9(2\bar{2}1)[110]38.9°$ tilt boundary. The experiment uses HRTEM (high-resolution transmission electron microscopy), and the micrograph occupies most of the figure. The inset is the *simulated image* of the structure predicted using the EAM. The inset and the experimental image agree well. The marks (+) indicate the centroids of the spots predicted by the EAM. (From Mills et al. [19].)

of lower overall density so that one might expect these effects to play a role. That the EAM results are so similar to pair-potential results suggests that the overall density at the boundary is close enough to bulk values that pair potentials still provide a reasonable treatment of the structure and energetics.

Along these lines, Foiles [15] investigated the role that the many-body interactions played in the computed structure of the $\Sigma 13[001]$ symmetric twist boundary in Au (discussed in section 5.1). He did this by constructing the effective pair potential that best approximates the EAM interactions and then recomputing the positions. The positions computed by the two methods were very similar suggesting that the many-body contributions do not play a crucial role in the structure of this boundary. The main difference between the results is that the expansion normal to the boundary is somewhat greater for the case of the pair interactions than for the full EAM interactions suggesting that the EAM allows for a somewhat greater overall density at the boundary.

The EAM predictions for the structures of the $\Sigma 99$, $\Sigma 9$, and $\Sigma 11$ tilt boundaries in Al were also compared to the structure predicted from a first-principles pair potential [16–18]. The match between the experimental and calculated images was good for both the EAM and pair-potential structures, with the EAM being in better agreement with experiment. The small differences in the structure of grain boundaries between the many-atom EAM calculation and the pair potentials indicate that, *for grain boundary structure*, the many-atom interactions are important but not overwhelmingly so.

5.3. Elastic properties of grain boundaries

Some investigations of the elastic properties of grain boundaries have also been carried out by Wolf et al. [101,102] and by Adams et al. [103]. In these calculations the bi-axial Young modulus (response to tension or compression applied normal to the boundary) and the shear modulus for shear in the plane of the boundary were computed. The results indicate that the shear moduli of grain boundaries are substantially smaller than for the bulk material. In contrast, the Young modulus for stresses normal to the boundary was found to be larger than the bulk.

These results were compared by Adams et al. to the changes in the elastic constants of the bulk crystal under strain. This comparison is based on the observation that a common structural feature of grain boundaries is an overall expansion of the material normal to the boundary. Thus the grain boundary may be related to a region under tensile strain but with no Poisson contraction in the plane of the boundary. These elastic constants are not available from experiment since the experimental results always include the Poisson contraction. The EAM was used to compute the change in the elastic constants with strain both for the experimental conditions and without Poisson contraction. It was found that for experimentally accessible strains the EAM reliably predicted the change in elastic constants with strain. For the case of no Poisson contraction, which is the case that should parallel what happens at a grain boundary, it was found that tensile strain increased the Young modulus but decreased the shear moduli. This is exactly the same trend found for the change in the elastic constants of the grain boundaries.

It should be noted that while this analogy predicts the sign of the changes in the elastic constants at a grain boundary, it is not very successful in quantitatively predicting the magnitude of the change. It should also be noted that the work by Wolf et al. [102] showed that these general conclusions did not depend on the use of the EAM energy expressions: the same qualitative results were obtained using simple pair interactions.

5.4. Thermal effects at grain boundaries

Foiles [104] has used the EAM to investigate the possibility of a thermal roughening transition occurring at a high-angle grain boundary. In particular, the finite-temperature equilibrium properties of the $\Sigma 5[001]$ twist boundary in Au were computed. In this boundary, the transition between the two crystals corresponds to a rotation of a quartet of atoms in the unit cell. It was found from energy-minimization calculations that it costs relatively little energy to displace the boundary plane by a plane in a single unit cell of the boundary thus producing a non-planar interface. Further, the interaction between the unit cells is weak as long as the position of the boundary does not vary by more than one plane between adjacent boundaries. It is possible to map the energetics of the distribution of boundary positions onto a model that is identical to the solid-on-solid models used to study surface roughening [105]. The parameters entering this model could then be determined by fitting the energetics of a variety of structures containing different distributions of boundary positions and the roughening transition temperature for the grain boundary can be computed from the known solution of the solid-on-solid model. Unfortunately, the quantitative values of the parameters depended strongly on the particular EAM functions used for gold so that the transition temperature is predicted to occur at either 100 or 500 K depending on the interactions used. In either case, the results show the possibility of such a roughening transition occurring at experimentally accessible temperatures. Finally, the effect of such a roughening transition on

the X-ray diffraction from the boundary was estimated and it was found that it would correspond to the extinction of certain grain boundary reflections. This would provide a possible means of detecting this transition. A better means of observing this transition would be grazing-angle diffraction since this is sensitive to the position of the boundary normal to the overall boundary plane.

6. Surfaces

Metal surfaces have provided a convenient proving ground for the EAM. Enough accurate measurements are available for some fundamental properties (e.g., surface relaxations) that close comparison to experiment is available. At the same time, there exist enough unusual phenomena, such as reconstructions and phase transitions, that the EAM has provided a useful tool for investigating new physics.

The EAM is seen to be capable of describing metal surfaces adequately; the key here is the role of the many-body interactions incorporated in the model. The reader is reminded of the discussion in section 2.2, where it is demonstrated how the effective interatomic interactions are influenced by the environment.

With this in mind, we discuss here the following topics: (1) energies and relaxations of unreconstructed surfaces; (2) surface phonons; (3) ordering and phase transition of H/Pd(111); (4) structural phase transition of Au and Pt(110); and (5) adatom clusters on Pt(100). In all of these examples, it is possible to view the predicted trends in terms of many-atom interactions, or in terms of coordination effects, or in terms of embedding functions. Within the EAM, the different pictures are all closely related.

Most of the calculations reported in this section were done using the functions from Foiles et al. [3].

6.1. Surface energies and relaxations

The energy and structure of the (1×1) low-index surfaces of Cu, Ag, Au, Ni, Pd, and Pt were obtained. The calculations were performed by minimizing the total energy of thick slabs with (100), (110), and (111) surfaces.

The results for the surface energies are presented in table 8. Generally, the surface energies are systematically too low, though the ordering with respect to face is correct. The error in the absolute surface energy can be traced back to neglecting the slope of the background density experienced by the surface atoms [5].

Table 8
Calculated surface energies of the low-index faces and the experimental average surface energy [106] in units of erg/cm^2. The theoretical results are from Foiles et al. [3]

Face	Cu	Ag	Au	Ni	Pd	Pt
(100)	1280	705	918	1580	1370	1650
(110)	1400	770	980	1730	1490	1750
(111)	1170	620	790	1450	1220	1440
experimental (average face)	1790	1240	1500	2380	2000	2490

Table 9
Relaxation of the top-layer spacing Δz_{12}, and of the second-layer spacing Δz_{23}, for the low-index faces. For the sake of comparison, these values are calculated for unreconstructed geometries. Distances are expressed in Å. From Foiles et al. [3]

Face		Cu	Ag	Au	Ni	Pd	Pt
(100)	Δz_{12}	−0.03	−0.04	−0.13	−0.00	−0.09	−0.14
	Δz_{23}	−0.01	−0.00	0.01	−0.00	−0.00	0.01
(110)	Δz_{12}	−0.06	−0.07	−0.22	−0.03	−0.16	−0.24
	Δz_{23}	0.00	0.01	0.03	0.00	0.02	0.04
(111)	Δz_{12}	−0.03	−0.03	−0.10	−0.01	−0.07	−0.11
	Δz_{23}	−0.00	0.00	0.02	0.00	0.01	0.02

The change in the interlayer spacings, Δz, computed for the relaxed surface geometries relative to the spacings for the truncated bulk geometries are presented in table 9. Note that all the top-layer spacings show a small contraction. Further, the rougher (110) surfaces show larger relaxations than do the smoother (100) and (111) faces. Both of these general features agree with the trends found in the experimental data. The relaxations are of the correct sign but generally smaller in magnitude than experiment [3].

Some other parameterizations of the EAM have given better quantitative agreement with experiment. For example, similar work, using different parameterizations of the EAM functions, was performed by Voter et al. [77,107,108]. Their work also investigated the multilayer relaxations. The agreement with experiment is encouraging. Work on Ni, Pd, Pt, and Au has been performed by Ning et al. [109]. Impressive results on the relaxations of these surfaces were obtained using the "equivalent-crystal" method [80,81], which is mathematically equivalent to the EAM. It would seem, therefore, that while qualitative agreement is possible within the general framework of the EAM, quantitative agreement depends somewhat on the details of the semi-empirical fitting.

For comparison to the results obtained by the related corrected effective-medium theory, the reader is referred to the paper by Raeker and DePristo [66], to the paper by Sinnott et al. [68], and to the review by Raeker and DePristo [67].

6.2. Surface phonons

Surface phonons are sensitive to the interactions between atoms at the surface. We have shown previously how well the EAM reproduces the bulk phonon spectrum. In this section we see how the change in coordination modifies the surface phonons.

Referring to section 4.1, the tensor $\mathbf{A}_{ij}$ represents the contribution to the force-constant tensor $\mathbf{K}_{ij}$ from the environment-dependent effective pair potential Ψ_{ij}. The other terms in $\mathbf{K}_{ij}$ include explicit many-atom contributions, which depend on the environment through the quantities $\boldsymbol{g}_i$. Just as the change in the effective interactions leads to shorter bond lengths and deeper potential wells at the surface, so will the charge density and its gradient modify the vibrational frequencies at the surface. The force-constant tensor predicted by the EAM is qualitatively different from that of a central-potential model. The structure of this tensor is made considerably richer by the inclusion of the many-body terms [49].

The bulk phonons of fcc metals were discussed in section 4.1, where good agreement between theory and experiment was found. Using the same procedure and the same func-

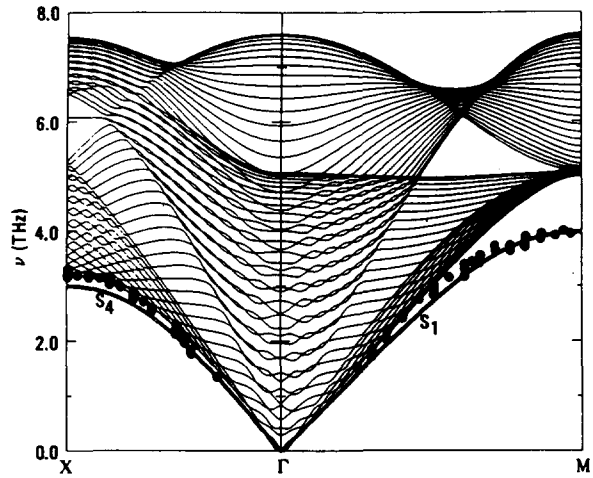

Fig. 8. Comparison of experimental and theoretical phonon frequencies on Cu(100). Only modes of even symmetry are shown. The experimental points are from Wuttig et al. [110,111]. The theoretical curves are from Nelson et al. [50].

tions, the normal modes of a 28-layer slab of Cu(100) were calculated [50]. Both ideal and relaxed (1×1) surfaces were considered. The calculated phonon modes for the relaxed surfaces are compared with experiment [110,111] in fig. 8. The Rayleigh modes S_1 along ΓM, and S_4 along ΓX have been measured, and are in excellent agreement with the calculated surface modes. It is worth noting that calculated splitting of the surface modes from the edge of the bulk modes is in better agreement with experiment than are the absolute values of the surface-mode frequencies.

The modifications of the force constants at the surface can be viewed in a two-step process. First, the bulk is truncated to create the unrelaxed (100) surface. Second, the bulk terminated surface is allowed to relax. The overall changes in the constants due to both processes result in a 15% softening of the intralayer force constants and a 15% stiffening of the interlayer force constants.

Calculations have also been performed on the (111) surfaces of Cu and Ag [49]. Over the past several years there has been considerable interest in the force-constant changes on (111) noble-metal surfaces. Measurements of the surface phonon dispersions have been performed with He-scattering and EELS experiments. The main point of controversy is the amount of softening of the intralayer force constants necessary to account for the observed position of the longitudinal-resonance mode. Values of the softening which range from 15 to 70% have been proposed. In their study of the Ag(111) surface, Bortolani et al. [112–115] used a force-constant model with central and angular interactions including up to second neighbors. The surface force constants were determined by fitting the measured inelastic-He-scattering cross sections. This procedure produced a 48% softening of the surface nearest-neighbor radial intralayer force constant for Ag and Cu. On the other hand, using a much simpler nearest-neighbor central-potential model, Hall et al. [116,117] reproduced the observed Cu(111) surface phonon spectrum and the inelastic-electron-scattering intensities with only a 15% reduction: this is a value similar to the one we found for Cu(100).

Detailed analysis of the EAM results for the (111) surfaces of Cu and Ag have been presented by Nelson et al. [49]. The results show that the force constants are modified at the surface by 10–15%. Also, features in the dispersion curves due to avoided crossings of surface

modes were observed. The existence of these avoided crossings may have contributed to the confusion when some of the experimental results were analyzed.

Similar work on surface phonons using the EAM has been carried out by Luo et al. [89,90,118]. Also, surface phonon lifetimes have been studied using molecular dynamics and the EAM [119]. Surface vibrational anisotropy and anharmonicity are discussed in Yang et al. [120].

6.3. *H/Pd(111)*

A joint experimental and theoretical effort [39] led to the discovery of two ordered phases for H adsorbed on Pd(111) near 100 K, the lowest critical temperature known for H on a transition-metal surface. Low-energy electron diffraction (LEED) experiments showed the existence of $(\sqrt{3} \times \sqrt{3})$R30° diffraction spots for a hydrogen coverage (Θ) near 1/3 and 2/3 ML. The system exhibits an order–disorder transition: the critical temperature at $\Theta = 1/3$ ML is 85 K, and for $\Theta = 2/3$ ML is 105 K.

The EAM was applied to the theoretical investigation of this system [40]. Remarkable agreement was found in that the EAM (without fitting to surface data) predicted not only the correct ordered structures for H/Pd(111) but also the critical temperatures to within better than 50 K.

An important conclusion of the joint theoretical and experimental work was that the hydrogen atoms are adsorbing on surface and *subsurface* three-fold sites. The term "subsurface" is here reserved for sites between the top two metal planes. It was shown that the subsurface octahedral sites are close in energy to the surface adsorption sites. The theory predicted that at very low temperatures the ordered structures are hexagonal arrays consisting entirely of hydrogen occupying *subsurface octahedral sites*, giving the $(\sqrt{3} \times \sqrt{3})$R30° symmetry at both coverages.

Monte Carlo simulations were performed for the relevant range of coverages and temperatures. The results of the simulations are compared to experiment in fig. 9. The agreement between the theoretical and experimental phase diagrams was extremely encouraging, especially considering that no adjustment of the theory was made to fit to surface properties.

The source of the H–H interaction in the framework of the EAM is easily understood. We can turn directly to the effective interactions calculated in eqs. (6). However, to illuminate the nature of the interaction, we will re-derive the effective interactions in a slightly different way.

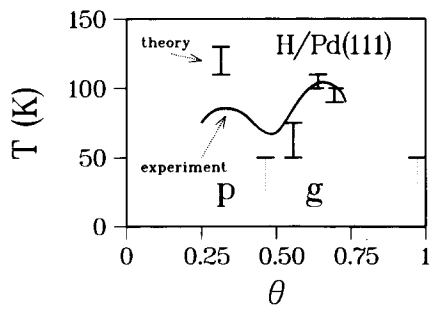

Fig. 9. Calculated and experimental phase diagrams for H/Pd(111). The "p" denotes the "primitive" $(\sqrt{3} \times \sqrt{3})$R30°-1H structure (i.e. $\Theta = 1/3$ ML), and the "g" denotes the "graphite-like" $(\sqrt{3} \times \sqrt{3})$R30°-2H structure (i.e. $\Theta = 2/3$ ML). The experimental results are from Felter et al. [39]. The theoretical results are from Daw and Foiles [40].

For simplicity, consider the interaction of hydrogen atoms occupying only the surface sites. On the clean surface, each Pd atom has an embedding energy of $G_{Pd}(\rho_S)$, where ρ_S is the electron density "seen" by a surface Pd atom. An adsorbed H atom contributes a density ρ_H to three neighbors on the Pd surface, each of which now has an embedding energy of $G_{Pd}(\rho_S + \rho_H)$. Nearest-neighbor hydrogen atoms share two atoms in the Pd substrate, each of which has an embedding energy of $G_{Pd}(\rho_S + \rho_H^{(1)} + \rho_H^{(2)})$ where the superscripts denote the two different hydrogen atoms. Expanding this last embedding energy in a Taylor series, assuming the ρ_H to be small compared to ρ_S, and subtracting out the single-atom adsorption energies, gives a nearest-neighbor interaction energy of $2G''_{Pd}(\rho_S)\rho_H^{(1)}\rho_H^{(2)}$, where the factor of 2 comes from the number of substrate atoms that have two H nearest neighbors. This interaction is simply part of the effective trio interaction in eq. (6b). Because $G''_{Pd} > 0$ and $\rho_H > 0$, this interaction is repulsive. Repeating the argument for second-nearest-neighbor hydrogen atoms gives an interaction of $G''_{Pd}(\rho_S)\rho_H^{(1)}\rho_H^{(2)}$ because in this case only one substrate atom has two H neighbors. This argument roughly accounts for the ratio of first- to second-nearest-neighbor interactions. Further, since second- and third-nearest neighbors share the same number of Pd atoms, their pair energies should be, and are, similar. Thus, the EAM naturally leads to the prediction of a substrate-mediated H–H interaction. The nature of this interaction is different from that investigated by other workers [121–124]. In the EAM, the significant H–H interactions are short-ranged, being most significant when two hydrogen atoms neighbor the same substrate atom.

More recent work [41] investigated the interactions between H atoms on Ni(111) and on Pd(100). For H/Ni(111) the binding-energy difference between the two three-fold sites was very small. As expected due to the very small separation, at nearest-neighbor sites there was an extreme repulsion. Hydrogen pairs at second- and third-neighbor separations have repulsive interactions on the order of a few meV. The energies for the ordered patterns were consistent with the isolated pairs (i.e. multi-site effects were not significant). The interactions are smaller than expected from experiment, and the (2×1) ordering is predicted instead of the observed [125] graphitic (2×2). For H/Pd(100), the interactions have realistic signs and orders of magnitude, but (2×1) ordering is predicted rather than the observed c(2×2) [126].

6.4. Au and Pt(110)-(1 × 2)

Theoretical and experimental results (see references in Daw and Foiles [36] and Foiles [33]) agree that the (110) surfaces of Au and Pt both reconstruct to a structure with (1×2) symmetry. Moreover, the (1×2) structure has been observed experimentally to undergo a reversible transformation to a "(1×1)" structure. Careful LEED measurements on Au and Pt(110) have shown that the transformation is due to a disordering of the missing-row structure. The critical temperatures for Au [127] and Pt [128] have been measured at 650 and 960 K, respectively.

Before it was clear that the (1×2) surface had a missing-row structure, several other candidate structures were proposed. Calculations with the EAM demonstrated that the missing-row structure is indeed lower in energy than the (1×1) structure for both Pt and Au(110) surfaces [33,36]. The other candidate structures were calculated to be much higher in energy. At about the same time the experimental analyses seemed to converge on the same conclusion.

The energy difference between the (1×1) and (1×2) (missing-row) structures was computed for Cu, Ag, Ni, and Pd as well, and is presented in table 10. Note that the energy differences are only slightly changed by the relaxation of the atomic positions. This result is

Table 10
Surface energy difference, $\Delta E = E((1\times2)) - E((1\times1))$, between the reconstructed missing-row surface and the unreconstructed (110) surface computed both with the atoms in the bulk positions (unrelaxed) and for the fully relaxed geometries. The energies are in meV/Å^2 (1 meV/Å^2 = 16 erg/cm^2). From Foiles [33]

Metal	ΔE (unrelaxed)	ΔE (relaxed)
Cu	1.2	1.1
Ag	−0.5	−0.4
Au	−2.3	−1.8
Ni	1.4	1.3
Pd	−0.6	−0.4
Pt	−2.9	−2.1

rather surprising since the energy gained by relaxing the atomic positions ranged from 1 to 13 meV/Å^2 – larger than the energy differences between the reconstructed and unreconstructed surfaces. These energy differences correctly predict that Au and Pt should reconstruct and that Ni and Cu should not. However, they also predict that Pd and Ag should reconstruct, in contradiction with experiment, though the computed energy differences are small.

The reconstruction of the (110) surfaces raises the interesting and important question of why only certain of the fcc metals undergo the reconstruction. The EAM provides a simple framework within which that question can be addressed. Recall that the calculated energy differences between the unreconstructed and missing-row surfaces are the same for the fully relaxed atomic geometry as for the case where the atoms are on ideal lattice sites. Thus it will suffice in this case to compare the energetics of the surfaces with the atoms on ideal sites. This ability to ignore the relaxations simplifies the analysis.

Ignoring the relaxations, it is a simple matter now to apply the concepts of the effective pair and trio interactions at the surface. This allows a simple qualitative comparison of the energetics of the missing-row and unreconstructed surfaces by simply comparing the relative number of different pair and trio interactions. The number of nearest-neighbor pairs per unit area is the same for both of these surface geometries. Since the bulk of the energy comes from the nearest-neighbor pair interactions, this explains why the two structures have similar energies. The differences between the two structures result from more distant neighbors and trio interactions. There are fewer second-nearest-neighbor pairs for the missing-row surface. Since the effective pair-interaction term is attractive, this favors the unreconstructed surface. (For this reason any pair-interaction model with purely attractive interactions will always favor the unreconstructed surface.) On the other hand, the number of nearest-neighbor triples per unit area is less for the missing-row surface. (A nearest-neighbor triple is a group of three atoms such that two of the atoms are both nearest neighbors of the third atom.) Since the effective three-body interactions are repulsive, the trio interactions favor the missing-row structure. To first order, the determination of the preferred structure is thus a competition between the attractive pair interactions at second-neighbor distance and the repulsive three-body interactions at nearest-neighbor distances.

The importance of the three-body interactions suggests a correlation between the tendency to undergo the (1×2) missing-row reconstruction and the curvature of the embedding function (see eq. (6b)). The curvature of the embedding function is indeed stronger as one moves down the column (Ni, Pd, Pt, for example). Thus, we conclude that three-body interactions are more important for Pt than for Ni (as was concluded also from table 1). This

Table 11
Geometrical parameters describing the relaxed surface geometries of Au(110)-(1×2) (missing row). Comparison is made between EAM, LEED, and MEIS. Δd is the change in interlayer spacing, Δp is the row pairing, and b is the buckling (see Foiles [33] for precise definitions). All distances are in Å

	Δd_{12}	Δd_{23}	Δd_{34}	Δp_2	Δp_4	b_3
EAM [33]	−0.21	−0.07	−0.01	−0.07	0.08	0.11
LEED [132]	−0.29	0.03	0.03	0.14		0.24
MEIS [133]	−0.26	0.06		(< 0.1)		0.20

shows up in the environmental dependence of the effective pair interaction: from fig. 3 we can see that this is much stronger for Pt than for Ni.

The (1×2) missing-row surface can also be viewed as a series of small (111) faces, suggesting the possibility of forming similar structures with larger (111) facets. In particular, a series of such structures can be envisioned that have $(1 \times n)$ periodicities where the troughs in the missing-row structure are simply made deeper by creating larger (111) facets. In the limit of large n, the energy of this surface is $\sqrt{3/2}$ larger than that of the (111) surface. (The factor of $\sqrt{3/2}$ accounts for the angle between the (111) micro-facets and the average (100) surface orientation.) Using the computed energy of the (111) surfaces, the energy of large-n surfaces is found to be greater than that of the (1×2) for both Au and Pt. For moderate n, the energy of the surfaces must be computed explicitly. For Pt, the lowest energy is obtained for $n = 2$, the missing-row structure. For Au, however, the $n = 3$ and $n = 4$ surfaces have slightly lower energy than the $n = 2$. "Glue-model" calculations [129] place the (1×2) slightly more favored than the (1×3) or (1×4). Experimentally, it is possible to create ordered surfaces with the (1×3) reconstruction [130,131].

The relaxed geometries computed with the EAM for the missing-row structure of Au and Pt(110) are compared to the LEED and medium-energy ion scattering (MEIS) results in tables 11 and 12 with good agreement. Many of the features of the computed structure agree with that determined experimentally. The top-layer atoms are relaxed into the surface and the atoms in the third layer are buckled. There is some disagreement between the two types of experiments as to the row-pairing. Generally, the theory agrees about as well with experiment as the two types of experiments agree with each other.

The experimental evidence indicates that the missing-row reconstruction undergoes a phase transition at higher temperatures. To understand the thermal properties of this reconstruction, equilibrium Monte Carlo simulations were performed on a (110) slab [34]. The simulation included both small jumps representing vibration/relaxation and larger jumps to unoccupied sites. The results indicate the existence of an order–disorder phase transition. The resulting structure factor for the Au $(0, \frac{1}{2})$ peak is plotted in fig. 10, and shows the transition temperature to be around 570 K. This is in excellent agreement with the experi-

Table 12
Same as table 11, but for Pt(110)-(1×2) (missing row)

	Δd_{12}	Δd_{23}	Δd_{34}	Δp_2	Δp_4	b_3
EAM [33]	−0.25	−0.07	−0.02	−0.05	0.08	0.11
LEED [134]	−0.26	−0.18	−0.12	0.13	0.24	0.32
MEIS [135]	−0.35	+0.08		0.0		0.10

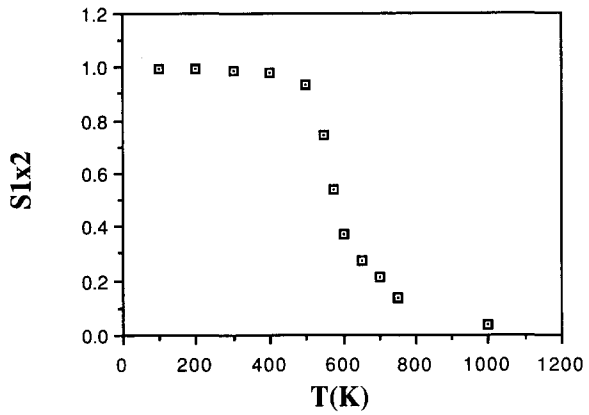

Fig. 10. The theoretical structure factor at $(0, \frac{1}{2})$ as a function of temperature for Au(110). The theoretical critical temperature is 570 K, in excellent agreement with the experimental value of 650 K. (From Daw and Foiles [34].)

mental value [127] of 650 K, *especially considering that only bulk data were used in determining the semi-empirical functions*. In this sense, these calculations represent the first quantitatively realistic *prediction* of the order–disorder transformation of a surface reconstruction.

The calculations for Pt(110) show a behavior similar to Au, except that the predicted transition temperature was about 750 K. These calculations stimulated experiments on Pt, and the recently published results [128] show a critical temperature of 960 K. As one would expect from semi-empirical methods like the EAM, the general trend of increasing critical temperature from Au to Pt agrees with experiment.

We have also calculated the $(0, \frac{1}{2})$ spot width for Au(110), parallel and perpendicular to the rows, as a function of the temperature. The temperature dependence is similar to that for the experimental LEED spot width, which is fairly constant below T_c and then increases rapidly with increasing temperature. The current theory shows, additionally, that the spot is not circular above T_c: the disorder perpendicular to the rows is stronger than that parallel.

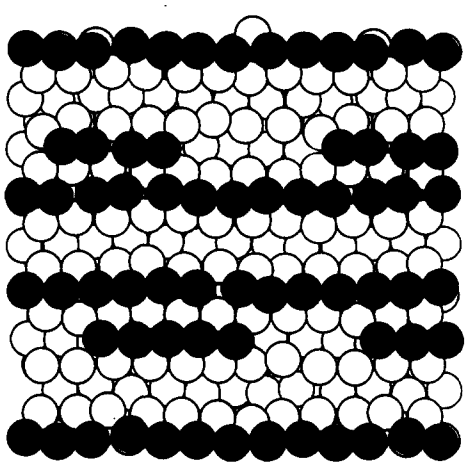

Fig. 11. Snapshot of a randomly chosen configuration from the Monte Carlo simulation of the Au(110) surface showing structure typical at a temperature slightly above the critical temperature. All atoms are Au atoms, with the "adatoms" darkened for illustration. (From Daw and Foiles [34].)

The picture that emerges is as follows. Below the critical temperature, the rows are generally long and coordinated but with some defects present. Well above the critical temperature, short-range order persists in the form of short chains of atoms along the [1$\bar{1}$0] direction but with little coordination among the rows. This is confirmed by snapshots of the Monte Carlo simulations, an example of which is shown in fig. 11.

The persistence of the chains (indeed even the existence of the missing-row reconstruction) suggests that the "adatoms" (i.e. the atoms forming the reconstructed layer) experience attraction for each other along the rows and effective repulsion across the rows. Again, this can be visualized in terms of effective pair and trio interactions. Along the row direction, neighboring atoms are at nearest-neighbor distance. The direct nearest-neighbor pair interaction is strongly attractive. There is also a substrate-mediated interaction, where the adatoms form a trio with a substrate atom. For every nearest-neighbor pair of adatoms, there are two trios formed with substrate atoms. Across the rows, the atoms interact at second-nearest-neighbor distance, so the direct pair interaction is much weaker. However, the trios are still present. The competition between the pair and trio interactions makes the net nearest-neighbor interaction attractive and the net second-nearest-neighbor interaction weakly repulsive [34].

As an additional note, the Monte Carlo simulations showed that relaxations and vibrations were significant. In fact, inclusion of the relaxations and vibrations was essential for the accurate calculation of the critical temperature. (Calculations that inhibited these effects yielded transition temperatures twice those found in the simulations.) This result has two major implications. First, the effective interaction between atoms is strongly modified by relaxations, which was studied in detail by calculating the energetics of adatom pairs with and without relaxations. Second, lattice gas calculations [127] traditionally neglect the effects of relaxations and vibrations. Therefore, lattice gas simulations must be carefully interpreted.

6.5. Adatom clusters on Pt(001)

The interactions of metal adatoms can be studied systematically by depositing adatoms onto the tip of a field ion microscope. The stability of various cluster geometries can then be studied as a function of the number of atoms in the cluster. In a joint experimental and theoretical effort, the stability of Ni, Pd, and Pt clusters on a Pt(100) substrate was examined [51,52].

The EAM was used to calculate the energy of various structures of Pt clusters on Pt(100). Two geometries were found to be important; a linear chain of atoms arranged along a [011] direction and close-packed-island arrangements. Table 13 shows the preferred geometry for clusters of up to six atoms. For clusters larger than six atoms, an island configuration was

Table 13
Preferred structure of the various small clusters of Pt adatoms on Pt(100). The competing structures are a linear cluster and an island cluster of specified size. The energy difference is between the preferred structure and the high-energy structure computed with and without relaxations. The energies are in meV. From Schwoebel et al. [51]

Size	Stable geometry	ΔE (relaxed)	ΔE (unrelaxed)
3	linear	159	−1
4	island	52	438
5	linear	32	-462
6	island	240	915

always preferred. Note that the calculations predict an alternation between the linear and island structures as the size of the cluster increases. Such an oscillation had not been seen before. Table 13 also lists the computed energy difference between the two alternate geometries including all relaxations. (The unrelaxed values will be discussed below.) In addition, the seven-atom cluster was studied. The preferred structure is the six-atom rectangle with the seventh atom in any of the sites next to one of the corner atoms of the rectangle and not next to the center atom of the long side of the rectangle.

The experimental observations of the cluster geometries confirm the calculated results shown in table 13. Clusters of three and five atoms always take a linear shape after annealing and clusters of four and six atoms always form a close-packed island after annealing. In addition, the seven-atom cluster has also been observed. The seventh atom of the cluster was always found next to one of the corner atoms and never next to the central atom of a side, in accord with the theoretical predictions.

One of the interesting features of the theoretical calculations of the cluster energies is the importance of relaxations. The last column of table 13 shows the energy differences between the two cluster structures computed with the atoms on ideal lattice sites. Without relaxations, the close-packed-island geometry is always preferred over the linear arrangement. Further, the contribution of relaxations to the energy difference is larger than the actual energy difference. Thus the inclusion of relaxation is crucial to the accurate calculation of the energetics of clusters.

The adatom energetics have sometimes been modeled by pair-interaction lattice models. The energetics obtained from the EAM including relaxations were used to determine two-, three-, and four-body interaction parameters. It was found that the three- and four-body interaction terms are not negligible in this case. In particular, the four-body interaction was found to be attractive by 163 meV. Therefore, it is important to consider more than pair interactions when modeling the energetics of the adatoms. Generally, however, the nearest-neighbor pair interaction is attractive, while the second-neighbor interaction is repulsive. This result is due to substrate-mediated interactions similar to the interactions on the (110) surface as discussed in section 6.4.

Wright et al. [52] continued this work by considering clusters of Pd and Ni adatoms on Pt(001). For Pd/Pt(001), the results were very similar to those for Pt/Pt(001): the stable configurations were predicted to be close-packed islands except for three adatoms, for which a linear chain was the predicted stable configuration. These results again agreed very well with FIM observations. For Ni/Pt(001), the results were quite different from Pt or Pd/Pt(001). For Ni, the stable configurations were predicted to be linear chains for all numbers of adatoms. The origin of this difference can be traced to the different bond lengths between the metals, as reflected in the different lattice constants. The importance of substrate relaxations was also investigated, and it was found that substrate relaxations play a significant role in determining the relative stability of linear versus close-packed structures.

7. Alloys

The EAM has been applied to the study of compositional variations that can occur near defects in alloys. The advantages of the EAM over other approaches for these calculations are two-fold. First, the formulation of the EAM in terms of the local electron density makes the extension of these ideas to the case of alloys straightforward. The interaction of the atom with the electron gas does not depend on the origin of the electron gas (i.e. the specific chemical

identity of the various neighbors); rather it is assumed to depend only on the local electron density. The effect of changing the chemical identity of the neighbors only enters this part of the problem through the change in the electron densities. The advantage of this assumption is that the embedding function that is used for the case of pure metals should still be valid for the case of alloys. This makes the application of this method to alloys relatively simple.

The other advantage of using the EAM relates to the computational simplicity of the method that allows one to perform atomistic simulations. There are many factors that enter into the energetics of alloys near a defect. One of these is sometimes referred to as the chemical effect, which represents the difference in the bond strengths between different chemical species. This effect is what bond-breaking models of the energetics focus on. There are other contributions to the free energy that can also be important that require the explicit consideration of the atomic positions. One is the interaction of the chemical species with the local stress fields at the interface (sometimes referred to as the "size effect"). This contribution is hard to incorporate in lattice models, but is incorporated naturally in atomistic models. Vibrational contributions to the free energy can also be important. Again these are included naturally in finite-temperature atomistic simulations such as Monte Carlo. Finally, at finite concentrations, the interactions between the chemical species can lead to ordering effects. These can be treated directly by using Monte Carlo simulations.

One should also be aware of the possible errors in treating certain alloys with the EAM. In addition to the restrictions mentioned in previous sections for elemental metals, the additional complexity added by alloying additions must be treated with caution. Large charge transfer in an alloy will not be treated well in the EAM. And, as before, any effects arising because of subtleties in the Fermi surface have been completely ignored in the EAM. These caveats must always be kept in mind. However, we believe that for the situations presented in this review these restrictions are obeyed.

A variety of examples of applying the EAM to alloys will be presented: (1) surface segregation in the dilute limit; (2) surface segregation in Ni–Cu; (3) surface segregation and ordering effects at finite concentration; and (4) segregation at grain boundaries.

The first is the case of surface segregation in the dilute limit. This calculation allows the characterization of the EAM results without the complication of concentration effects. Even in the dilute limit, it is possible to see the presence of interesting concentration oscillations in some systems. Moving away from the dilute limit, the Ni–Cu system is expected to be dominated by the bond-strength effects and so this work provides a test of the ability of this method to treat this aspect of the problem. We then consider some examples of ordering effects at finite concentration. These include the short-range compositional order in Pd–noble-metal surfaces, the formation of ordered surface alloys in the Cu–Au system, and the reduction of order that occurs at grain boundaries in the ordered intermetallic compound Ni_3Al. Finally, we explore the relationship between the segregation at grain boundaries in two systems (Ni–Cu and Pt–Au) and the effects of local strain fields at the boundary.

7.1. Dilute surface segregation

Taking the dilute limit simplifies the study of segregation in alloys. Frequently the dilute results point to interesting results that should be present at higher concentrations. With that in mind, we first present the results of the EAM for dilute alloys.

Foiles, Baskes, and Daw [3] studied dilute surface segregation in the binary alloys composed of the fcc metals Cu, Ag, Au, Ni, Pd, and Pt. To test the ability of the EAM functions to correctly predict segregation, the zero-temperature energetics of an impurity

Table 14
The energy of a single impurity in the first and second atomic layers of a (100) surface relative to the energy of the impurity in the bulk of the host material. The energies are given in eV, and include relaxations. The first line is the energy in the first atomic layer and the second line is the energy in the second atomic layer. From Foiles et al. [3]

	Host					
	Cu	Ag	Au	Ni	Pd	Pt
Cu		0.10	0.15	−0.18	0.03	−0.04
		−0.01	−0.07	0.02	−0.12	−0.09
Ag	−0.46		−0.07	−0.75	−0.25	−0.44
	−0.04		−0.03	−0.03	−0.15	−0.06
Au	−0.40	0.11		−0.94	−0.18	−0.49
	−0.01	0.01		−0.03	−0.08	0.04
Ni	0.11	0.11	0.15		0.02	−0.01
	−0.03	−0.03	−0.13		−0.19	−0.20
Pd	−0.13	0.24	0.21	−0.62		−0.23
	0.04	0.02	0.04	0.02		0.12
Pt	0.15	0.42	0.38	−0.32	0.22	
	0.01	−0.01	−0.05	0.00	−0.10	

atom near a (100) surface were computed. Table 14 presents the energy of a substitutional impurity atom in either the first or second atomic layer of a (100) face of a pure metal slab computed relative to the energy of that substitutional impurity in the bulk. A negative value of this energy thus implies that the impurity in question will be enriched in that atomic layer. Of course, these energies are computed in the dilute limit and can change substantially if there is a significant concentration of the impurity near the surface. The utility of these numbers is that they indicate the segregating species and suggest the magnitude of the segregation.

The segregating species is known experimentally for 18 of the cases examined here [136–138]. In all of these cases, the calculations predict that the experimentally observed segregating species will be enriched in either the first or second atomic layer. There are two interesting features in these results. First, in many cases the sign of the segregation energy differs for the two planes. This reversal of sign suggests that the composition profile may oscillate in these cases. Such behavior was found in the study of the Ni–Cu system as discussed in section 7.2. Second, for Cu or Ni in Pd or Pt hosts, the segregation energy is larger for the second layer than for the first. This suggests rather interesting composition profiles for these cases, which is explored in the following.

7.2. Bond breaking (surface segregation in Ni–Cu)

The Ni–Cu alloy was studied through the full range of compositions by Foiles [42]. The functions used in these studies were tailored specifically for the bulk Ni–Cu system (as opposed to the functions of Foiles et al. [3,4], which were for several elements and their alloys – see table 2). The bulk properties of this alloy were studied by Monte Carlo simulations. These simulations showed that the excess enthalpy agrees well with the thermodynamic data. The deviations of the lattice constant from Vegard's law obtained from the EAM have a small positive value while experiments show a small negative deviation. However, it should be noted that the lattice constants are correct to within 0.03 Å over the entire composition range. Finally, the short-range order in the alloy was computed and found to be in good accord with the diffuse neutron scattering data.

To obtain a qualitative idea of the segregation, we examine the heat of segregation in the dilute limit. As expected, the segregation energy for Cu in Ni surfaces is negative and that for Ni in the first layer of Cu is positive. This result is in accord with the known segregation of Cu to the surface of these alloys. The segregation energy for Cu in the first layer of the Ni(100) surface has been determined experimentally by Egelhoff [139] using X-ray photoemission spectroscopy. His value for the heat of segregation is -0.43 ± 0.04 eV.

The EAM value was calculated with both sets of functions available. With the functions from Foiles et al. [3,4], this value is -0.18 eV (see table 14). With the functions from Foiles [42], which were tailored for the Ni–Cu system, the value is -0.43 eV. It is fair to say then that the EAM estimates the heat of segregation at about -0.3 eV, in reasonable agreement with experiment.

The surprising feature of the results is the heats of segregation to the planes just below the surface. Here the energies show that Ni is attracted to the second or third atomic plane, or equivalently that Cu is repelled from these planes. This oscillation of the heat of segregation suggests that the composition profile should not be monotonic. This prediction agrees with the experimental results of Ng et al. [140] using field ion microscopy. They observed a depletion of Cu from the near-surface atomic planes for a NiCu(5%) sample at $T = 800$ K.

The above heats of segregation are for the extreme dilute limits. Since these energies are fairly large, one expects that the surface layer will be strongly enriched in Cu for all bulk compositions. This change in local composition will affect the energetics of the atoms near the surface. Therefore, the above heats of segregation cannot be used to estimate surface compositions. To address this issue, Monte Carlo simulations have been performed at a temperature of 800 K. This temperature is in the range of the temperatures for the various experimental studies of this system and high enough so that equilibrium in the experiments is expected. Simulations have been performed for the three low-index faces for a variety of bulk compositions spanning the entire concentration range.

The layer-by-layer compositions computed from the simulations are presented in table 15, and the concentration of the first three layers of the (111) surfaces is plotted as a function of bulk concentration in fig. 12. The trends suggested by the segregation energies in the dilute limit are retained in these results. The first layer is almost pure Cu for all the compositions and crystal faces studied here. Further, there is a noticeable enrichment of Ni in the near-surface atomic layers.

Table 15
The calculated composition profile in % Cu for Ni–Cu alloys at $T = 800$ K. The subscripts refer to the atomic layers. From Foiles [42]

Face	X_{bulk}	X_1	X_2	X_3	X_4	X_5
(111)	4.8	89.4	3.0	4.0	5.0	4.8
	29.2	95.0	11.0	19.1	27.1	29.0
	55.2	96.2	21.3	43.2	56.9	57.0
	71.9	97.5	39.0	70.2	76.8	71.3
	93.3	99.1	79.3	93.8	93.6	92.8
(100)	25.0	97.5	11.7	11.6	18.6	23.5
	57.0	98.1	22.7	36.6	57.7	60.3
	73.9	98.7	38.6	60.9	78.1	75.8
(110)	29.1	99.1	36.8	14.1	19.8	27.0
	55.1	99.4	43.9	25.4	40.3	54.0
	72.0	99.7	55.8	44.3	64.8	76.3

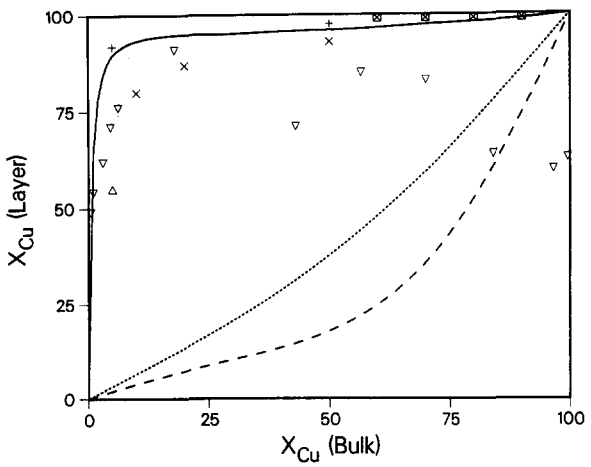

Fig. 12. The calculated Cu layer concentrations as a function of bulk composition at 800 K for the (111) surface of Ni–Cu alloys. The solid curve is the top layer, the long dashed curve is the second layer and the short dashed curve is the third layer. The points are the experimental values for the top layer from Webber et al. [141] (+), Brongersma et al. [142] (×), Brongersma et al. [143] (⊗), Ng et al. [140] (△), and Sakurai et al. [144] (▽). (From Foiles [42].)

There have been several experimental studies of the surface composition of Ni–Cu alloys including five studies appropriate to single-crystal (111) face [140–144]. The results of these experiments for the top-layer composition are compared with the theoretical predictions in fig. 12. In four of the five cases the agreement is good. The experimental situation is controversial for the case of alloys with high Cu content. Sakurai et al. [144] recently measured the segregation for Cu-rich alloys using FIM. They find lower levels of segregation than in previous studies for alloys with around 50% Cu. They also find a reversal of the segregation with Cu depleted from the surface for bulk composition of more than 90% Cu. Subsequent to these experiments, Brongersma et al. [142,143] measured the segregation of Cu-rich alloys using LEIS. They find surfaces that are enhanced in Cu in accord with our calculations and in disagreement with the work of Sakurai et al.

7.3. Compositional ordering

In addition to compositional variations with depth from the surface, segregating components may exhibit ordering (or clustering) within the plane of the interface. In the following sections, we will discuss work relating to: short-range order in the segregating species; long-range order in the segregating species; and loss of long-range order at an interface in an ordered alloy.

7.3.1. Example of short-range order: surface segregation in Pd–noble-metal alloys

The segregation behavior predicted using the functions of Foiles, Baskes and Daw [3] has been studied in some detail for a few of the binary systems. Foiles [45] studied the segregation and the surface short-range order of the alloys of Pd with the noble metals. These alloys are catalytically interesting because they combine a catalytically active element, Pd, with catalytically inactive elements, the noble metals. Such binary alloys are known to exhibit chemical selectivity in their catalytic behavior.

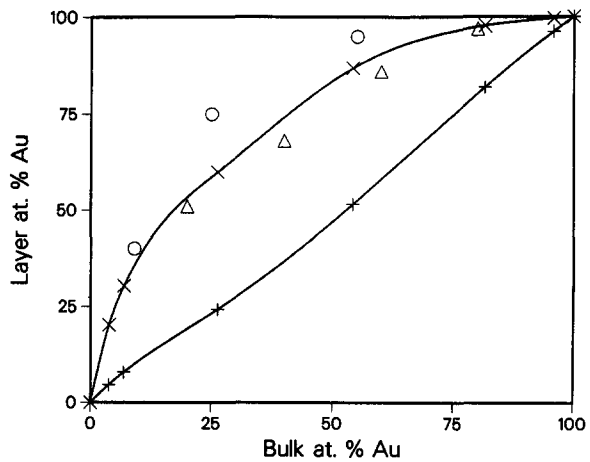

Fig. 13. The composition in at.% of the first (×) and second (+) atomic layers of the (111) surface of Pd–Au as computed by Monte Carlo simulations at 800 K. The triangles (△) represent ion scattering results for the surface composition of a polycrystalline sample at 873 K [145] and the circles (○) are ion scattering results for a polycrystalline sample at 773 K [146]. The lines are a guide to the eye. (From Foiles [45,46].)

In this study the composition profiles are computed at finite concentrations and at finite temperatures for the (111) surfaces. The results for the composition of the first two atomic planes of the (111) surface of the Pd–Au alloys at a temperature of 800 K are presented in fig. 13. The first atomic plane is seen to be enhanced in Au compared to the bulk while the second and deeper planes have compositions close to the bulk value. The first-layer compositions are compared to two different ion scattering measurements of the surface composition by Swartzfager et al. [147] for a polycrystalline surface at 873 K and by Hetzendorf and Varga [148] for a polycrystalline surface equilibrated at 773 K. While the experimental results are for a polycrystalline sample rather than the single-crystal (111) face of the calculations, the results indicate that the magnitude of the Au segregation predicted by the calculations is reasonable. It is also important to note that the segregation is found to be confined to a single monolayer at the surface. This result is in accord with the results of Hetzendorf and Varga [148] where it was found that significant segregation was observed with ion scattering (which is sensitive to just the surface layer) whereas with Auger spectroscopy (which samples several atomic layers) only slight segregation was observed. This experimental result implies that the segregation occurs in a very thin layer at the surface, in agreement with the calculations.

In addition to determining the composition profile of the surface, the simulations can be used to study the short-range order of the alloy surface. This study is of interest both for fundamental reasons and because the short-range order determines the relative abundance of compositionally different adsorption sites on a surface. It is thought that the presence of compositionally different adsorption sites is a factor that leads to the chemical selectivity of binary alloy catalysts. An important adsorption site on (111) surfaces is the three-fold hollow site located at the center of the triangle of nearest neighbors. For a binary alloy, four different configurations of these triangles of surface atoms are possible depending on how many atoms of each type are present.

The relative abundance of local clusters of different composition depends both on the overall composition of the surface as well as on the short-range order of the alloys in the

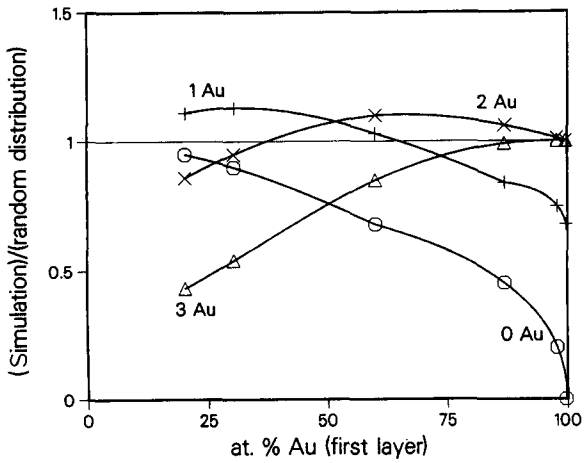

Fig. 14. The abundance of nearest-neighbor triangles on the (111) surface of Pd–Au alloys at 800 K which contain 0 (○), 1 (+), 2 (×), or 3 (△) Au atoms relative to the abundance based on a random distribution of the surface atoms. (From Foiles [45].)

surface layer. Since the excess enthalpies of all the alloys considered here are negative, these alloys are ordering alloys. That is, the short-range order favors placing atoms of different types on adjacent lattice sites. Thus one would expect that the abundance of triangles containing three atoms of the same element would be suppressed while the abundance of triangles containing a mixture of elements would be enhanced.

The computer simulations contain information on the short-range order of the alloy in addition to the average composition on each plane. The relative abundance of the different types of triangles has been studied quantitatively by counting the number of nearest-neighbor triangles with 0, 1, 2, or 3 noble-metal atoms that occur in the surface layer of the simulations. These values are then compared with the number that would be present if the noble metal atoms were distributed randomly in the top layer. In particular, if P_N^i is the probability of finding an N-atom cluster with i noble-metal atoms, then we can define a correlation function, g_N^i, by the relation

$$P_N^i = \left\{[N!/(N-i)!i!]\, x^i (1-x)^{N-i}\right\} g_N^i, \tag{9}$$

where x is the fraction of noble-metal atoms in the surface layer. The quantity in curly brackets is the probability expected for a random distribution so that g equals one if there is no correlation.

Fig. 14 presents the correlation function, g, for the abundance of each type of nearest-neighbor triangle found on the (111) surfaces of the Pd–Au alloy. The behavior found for the Pd–Ag and Pd–Cu alloys is very similar. For all compositions, the presence of trios containing either 0 or 3 noble-metal atoms is reduced as expected based on the bulk thermodynamics. The presence of triangles containing either 1 or 2 noble-metal atoms is enhanced. The behavior of these trio correlations can be understood based on the pair correlations as has been discussed by Foiles [45].

7.3.2. Example of long-range order: surface segregation in Cu–Au alloys

Besides short-range order, it is also possible for a surface layer to contain long-range order, as demonstrated by Foiles [47]. This work was motivated by experimental studies of the

deposition of Au on the Cu(100) surface. These studies showed the existence of a c(2 × 2) ordered structure after the deposition of 1/2 ML of Au [149–151]. The analysis of the LEED data shows that rather than an ordered overlayer of Au adatoms, the surface consists of a surface plane containing both Au and Cu with the Au atoms arranged in a c(2 × 2) pattern [151]. The second atomic plane was found to contain solely Cu. The surface layer was also found to be rippled with the Au atoms in the top layer positioned 0.1 Å higher than the Cu atoms. The separation of the first and second Cu layers was found to be expanded by 0.08 Å compared to the bulk spacing. These results are interesting because they suggest the existence of a stable ordered surface alloy. In this work, theoretical calculations are presented which support the results of the experimental studies of the (100) surface and determine the ordering on two other low-index surfaces, the (111) and (110).

During the initial stages of the deposition of Au on a clean Cu(100) surface, Au atoms will be placed as adatoms on the Cu surface. One must then determine whether the Au will prefer to form a layer on top of the Cu surface, mix with the Cu in a region localized to the surface, or simply diffuse into the bulk. To address this question the energy of a Cu(100) surface with a single Au adatom was computed and compared to the energy for a Cu surface with a Cu adatom and a Au substitutional atom in the surface layer. This energy difference corresponds to a process where the deposited Au atom exchanges with a Cu atom in the surface. It is found that the incorporation of the Au adatom into the surface is energetically favored by 0.14 eV. Thus the energetics favor the initial incorporation of the deposited Au into the surface layer. The energy of the Au atom in the surface layer is 0.40 eV below that of the substitutional in the bulk and the energy of the substitutional in the second atomic layer is 0.01 eV below its energy in the bulk (see table 14). Therefore, the initial Au atoms will be energetically bound to the surface atomic layer in accord with the experimentally deduced structure.

In order to determine the ordering, if any, of the Au atoms in the surface layer, Monte Carlo simulations were performed for slabs exposing the (100), (110), and (111) surfaces at a temperature of 300 K. The chemical potentials for the calculations were chosen so that there is only dilute Au content in the bulk of the slab. (The relative composition of the bulk material and the surface will be discussed below.) To avoid prejudicing the simulation results by the initial distribution of Au atoms, the slab initially contains only Cu and Au atoms are then created by the simulation. Figs. 15–17 show snapshots of randomly selected atomic configurations generated during the simulations for the (100), (111) and (110) surfaces respectively. For all three surfaces, the Au atoms are essentially confined to the surface atomic plane. For the (100) surface (see fig. 15) a clear c(2 × 2) arrangement of the atoms with a half monolayer of Au is seen. This agrees with the symmetry and coverage found in the experiments. For the (111) surface (see fig. 16), the ordered structure occurs with 1/3 of a monolayer of Au and a primitive $(\sqrt{3} \times \sqrt{3})$R30° structure. (The particular configuration shown contains a defect – namely, a Au site occupied by a Cu atom near the center of the figure.) The snapshots in fig. 17 of the (110) surface is from a simulation containing 4 times the surface area that was usually used. The majority of the surface shows a c(2 × 2) ordering of the Au atoms at a half monolayer but also contains a defected row. This kind of defect is seen in several snapshots of this surface.

The calculations also determine the relative compositions of the surface layers and the bulk material corresponding to thermal equilibrium at room temperature. For the (100) and (111) surfaces, there is a wide range of bulk compositions for which the surface composition is approximately 1/2 or 1/3 respectively. This indicates that these surface phases are particularly stable with respect to changes in stoichiometry. In addition, the composition of the

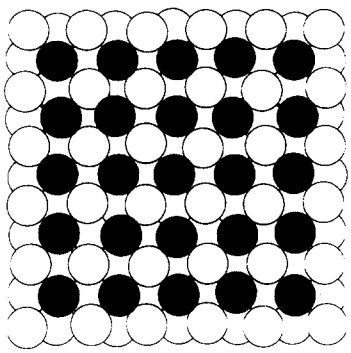

Fig. 15. A snapshot of a randomly chosen configuration from the Monte Carlo simulation of the (100) surface of Cu containing dilute amounts of Au showing the $c(2 \times 2)$ ordered structure. The filled circles are Au atoms and the empty circles are Cu atoms. The simulations are for a temperature of 300 K and a bulk Au content of 0.1 at.%. (From Foiles [47].)

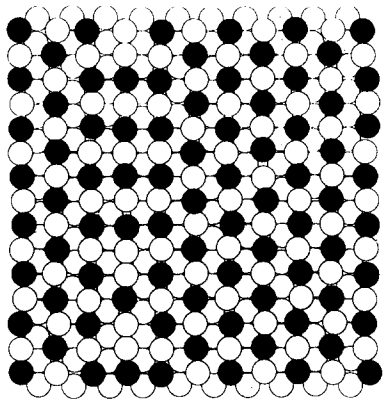

Fig. 16. As in fig. 15 except showing the arrangement of Au on the (110) surface for a bulk composition of 0.01 at.% Au. (From Foiles [47].)

second layer was found to be similar to that of the bulk for both of these surfaces. For the (110) surface, there is not a significant plateau at 1/2 ML – suggesting that the appearance of this ordered structure depends somewhat on bulk composition.

The calculations also give information about the detailed atomic positions at the surface. For all three of the surfaces studied here, the calculations show a rippled surface with the Au atoms sitting somewhat above the Cu atoms in the surface plane. For the (100) surface, the separation of the second and third atomic planes is within 0.005 Å of the bulk spacing. The spacing from the second atomic layer to the Cu atoms in the surface is 0.02 Å less than the bulk interplanar spacing and the spacing to the Au atoms is 0.16 Å greater than the interplanar spacing. This gives a rippling of 0.18 Å in the surface layer. The second atomic plane has no rippling. Wang et al. [151] find in their LEED analysis that the spacing from the second plane to the Cu atoms in the surface is expanded by 0.08 Å from the bulk spacing and

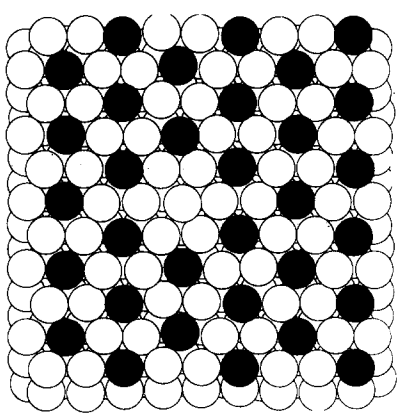

Fig. 17. As in fig. 15 except showing the arrangement of Au atoms on the (111) surface for a bulk composition of 0.1 at.% Au. (From Foiles [47].)

that the spacing from the second plane to the Au atoms is expanded by 0.18 Å from the bulk spacing. This gives a rippling of 0.1 Å in the surface plane. The theory and LEED analysis agree on the position of the Au atoms with respect to the bulk but the calculations place the Cu atoms in the surface plane 0.1 Å closer to the bulk.

These calculations have shown that the deposition of Au onto the (100) surface of Cu should result in the incorporation of the Au atoms into the surface atomic layer with the Au atoms arranged in a $c(2 \times 2)$ pattern. In addition, the surface should be rippled with the Au atoms residing above the Cu atoms. These results agree with recent LEED experiments. Also, the ordering of Au deposited on the (111) and (110) surfaces has been predicted. More generally, the calculations show that compositionally *ordered* surface layers of Au and Cu exist in equilibrium with a compositionally *disordered* bulk Cu containing dilute amounts of Au.

7.3.3. Loss of long-range order: segregation to grain boundaries in Ni_3Al

As a rather different example, we consider in this section the segregation of anti-site defects to grain boundaries. In this case, the bulk phase is an ordered alloy (Ni_3Al). The introduction of a different stoichiometry in the bulk causes anti-site defects to segregate to the boundary which in turn causes a loss of long-range order at the boundary.

Three different boundary geometries were considered in this study [21], a $\Sigma 5(001)$ twist boundary, a $\Sigma 13(001)$ twist boundary, and a $\Sigma 5(210)$ symmetric tilt boundary. The simulations were performed both at 500 K and at 1000 K. Simulations were performed for three sets of chemical-potential differences corresponding to a Ni-rich bulk, an Al-rich bulk and an ideal stoichiometric bulk.

The compositional structure determined by the simulations for the twist boundaries at ideal stoichiometry is very simple. The (100) planes of the Ni_3Al structure alternate between pure Ni and an equal mix of Ni and Al. At the two [100] twist grain boundaries, this alternating pattern of the (100) planes parallel to the boundary continues uninterrupted through the boundary. Thus the compositional ordering is the same that would be obtained by taking an ideal Ni_3Al crystal and rotating the two halves to form the boundary. This result is not surprising since the interactions favor the presence of Ni–Al nearest-neighbor pairs and this structure accomplishes that. The structure of the tilt boundary is more complicated. The atoms originally in the (210) plane on each side of the boundary combine to form one dense plane with little compositional order. The atoms in the next (210) plane on each side of the boundary have positions close to those in the bulk crystal.

The overall composition of the boundary region was studied as a function of the bulk composition. At the ideal 3:1 bulk composition, the average composition of the grain boundaries was also 3:1. For Ni-rich samples, the grain boundary region is found to have a further enhanced Ni concentration relative to the bulk and for the Al-rich samples, the boundary is enhanced in Al. This effect can be quantified in terms of the interfacial excess of one of the two components. The interfacial excess of Ni is defined as the difference per unit area of the boundary between the total number of Ni atoms in the sample (including the interface) and the number that would be present if the bulk composition is assumed throughout. The Ni excess computed at 1000 K was similar for the different boundaries studied and is approximately $-0.015/\text{Å}^2$ for a bulk composition of 74 at.% Ni, 0 for 75 at.% Ni and $0.012/\text{Å}^2$ for 76 at.% Ni. This behavior can be qualitatively understood by considering the energy to create anti-site defects near the boundary. (An anti-site defect corresponds to placing a Ni atom in a lattice site normally occupied by an Al atom or vice versa.) The anti-site formation energies for sites near the boundary are reduced by 0.2 to 0.4 eV for both

types of anti-site defects. Thus it is energetically favorable to create either kind of anti-site defect at the boundary rather than in the bulk material. Therefore, the change in composition of the boundary region can be thought of as being due to the binding of anti-site defects to the boundary region.

In addition to the overall composition of the boundary region, the compositional order of the boundary is also affected by the bulk composition. This is most easily seen for the twist boundaries. For boundaries that are Al-rich, the excess Al could either be placed in the Ni plane or in the Ni sites of the mixed composition plane. The simulations show that most of the Al goes to the Ni plane. For the Ni-rich case, one would simply expect to replace the Al atoms in the mixed composition plane with Ni atoms. However, the simulations indicate a reduction in the ordering within the mixed composition plane. For the $\Sigma 13$ boundary at a bulk composition of 24.5 at.%, there are three times more anti-site defects in the mixed composition plane than are required by the reduced Al concentration in that plane. In addition, the Ni plane in this boundary is found to contain 4 at.% Al atoms even though the system is deficient in Al. Thus the compositional ordering is reduced near the boundary in the case of Ni-rich alloys. It is important to note that this disordering effect is very localized. Only the planes immediately adjacent to the boundary are affected.

There is significant interest in whether the grain boundaries in this alloy are compositionally ordered or disordered. King and Yoo [152] have pointed out that compositional disordering at a boundary may affect the plastic deformation, in which dislocations impinge on a boundary. High-resolution electron microscopy has been used to search for such a disordered region in boron-doped nickel aluminide alloys. The results are inconclusive. Mackenzie and Sass [153] reported a large (~ 40 Å thick) region of compositional disorder at the grain boundaries. Mills [154] does not find a large region of disorder. His observations indicate that if there is compositional disorder at the boundary, it is confined to one or two planes on either side of the boundary. This conclusion is consistent with the very localized disordering seen in the above simulations (in boron-free material).

7.4. Segregation in strain fields

An interesting facet of segregation at grain boundaries is the role of strain. It is possible to view some boundaries as arrays of dislocations. In that case, it may be possible that the segregating species interact with the grain boundary dislocations. As examples of this effect, we consider segregation to: an edge dislocation; a twist grain boundary in Ni–Cu; and a twist grain boundary in Pt–Au.

7.4.1. Segregation to a sessile edge dislocation

In this section we examine the calculation of segregation at an edge dislocation in the Ni–Cu alloy system [44]. The particular dislocation studied has a Burgers vector of $(a/2)[110]$ and the dislocation line is along the $[1\bar{1}2]$ direction. In a fcc lattice this dislocation separates into two partials with Burgers vectors $(a/6)\langle 112\rangle$. Free surfaces are used in the remaining two directions. The chemical-potential difference was chosen to correspond to Ni with 10 at.% Cu and the temperature used in the simulations was 800 K.

The average composition as a function of position within the plane perpendicular to the dislocation line is presented in fig. 18. The most dramatic and important features of these results are the two peaks in the composition. The peaks are located at the centers of the two partial dislocations and have compositions of around 40 at.% Cu. This is a significant enhancement over the bulk Cu content of 10 at.%. The cliff on the front side of the peaks (as

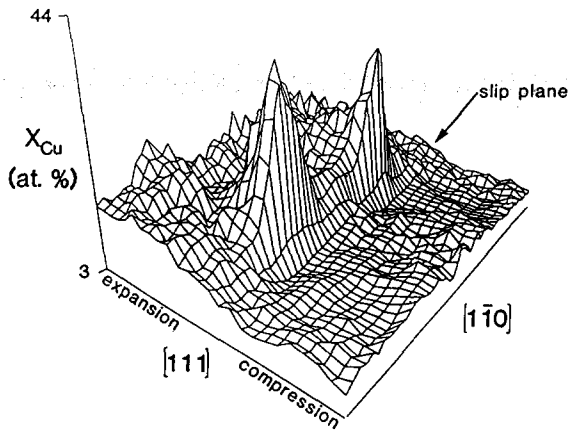

Fig. 18. Calculated Cu concentration of an $(a/2)[110]$ edge dislocation in Ni–10 at.% Cu at 800 K as a function of position perpendicular to the dislocation core. The length of the [111] axis is 50 Å and the length of the [1$\bar{1}$0] axis is 62.5 Å. The Cu enrichment occurs predominantly at the partial dislocation cores on the expansive side of the slip plane. (From Foiles [44].)

shown in the figure) is located at the slip plane of the dislocation. On the other side of the slip plane, there is a small depletion of Cu. The Cu enhancement occurs on the expanded side of the slip plane and the depletion on the compressed side. Note that the details of the composition profile away from the cores are not reliable in these calculations since the boundary conditions do not reflect the correct long-range strain field. It is important to note that there is significant segregation to the core of the dislocation. This is the region where treatments based on elasticity theory, such as the concept of a Cottrell atmosphere [155], cannot be applied. The ability to study the core region is the main power of this approach.

7.4.2. Segregation to (001) twist boundaries in Ni–Cu

The segregation to three different (001) twist boundaries in Ni–Cu has also been computed [22]. In particular, the $\Sigma 5$ (36.9°), $\Sigma 13$ (22.6°), and $\Sigma 61$ (10.4°) twist boundaries are simulated for bulk Cu concentrations of 10, 50 and 90 at.%. The simulations were performed at 800 K. The results for the overall composition of each of the three planes adjacent to the boundary are presented in table 16. In all cases the grain boundary region is enriched in Cu relative to

Table 16
Composition of the first three planes adjacent to the grain boundary computed by Monte Carlo simulations using the embedded-atom method. The net expansion (in Å) of the grain boundary normal to the interface is also listed. The statistical uncertainty in the compositions is ±1%. From Foiles [22]

	First plane	Second plane	Third plane	Net expansion
NiCu(10%)Σ5	74% Cu	22% Cu	11% Cu	0.60
NiCu(10%)Σ13	62% Cu	24% Cu	11% Cu	0.35
NiCu(10%)Σ61	41% Cu	27% Cu	15% Cu	0.44
NiCu(50%)Σ5	78% Cu	48% Cu	42% Cu	0.42
NiCu(50%)Σ13	74% Cu	52% Cu	44% Cu	0.29
NiCu(50%)Σ61	66% Cu	57% Cu	51% Cu	0.30
NiCu(90%)Σ5	95% Cu	90% Cu	90% Cu	0.32
NiCu(90%)Σ13	95% Cu	90% Cu	89% Cu	0.27
NiCu(90%)Σ61	92% Cu	91% Cu	90% Cu	0.20

the bulk Cu concentration and the change in composition is confined to the region within 3 to 4 atomic planes of the boundary. In addition, table 16 lists the net expansion normal to the boundary. This expansion is defined as the difference in the distance between two planes on opposite sides of the boundary for the system with the grain boundary and the distance for the same number of interlayer spacings at the bulk lattice constant. In all cases, there is an expansion of the boundary region and the amount of expansion is greater than can be accounted for by the increased concentration of Cu at the boundary. (Cu has a somewhat larger (3%) lattice constant than Ni.) This expansion is a general feature of grain boundaries.

There are two trends that are apparent from the results in table 16. First, the segregation is strongest for the higher-angle (lower-Σ) boundaries. A similar trend is found for the Pt–Au twist boundaries discussed in section 7.4.3. Second, the segregation is strongest for the Ni-rich alloy and weakest for the Cu-rich alloys. This latter observation is consistent with calculations of the dilute segregation energies performed for the $\Sigma 5$ boundaries. The dilute segregation energy is computed by comparing the energy of a single substitutional impurity located at a position at the grain boundary compared to its energy in the bulk material. For the case of a Cu impurity in Ni, the Cu is bound by 0.22 eV to the coincident sites of the boundary that comprise 1/5 of the boundary sites and is bound by 0.13 eV to the four equivalent non-coincident sites that comprise the remaining 4/5 of the boundary sites. For the case of a Ni impurity in Cu, the Ni is repelled from the boundary plane by 0.07 eV for both the coincident and non-coincident sites. These energies indicate that the segregation of Cu to the boundary is stronger for the case of pure Ni than for the case of pure Cu consistent with the trend observed for the concentrated alloys.

The segregation at the boundary in the concentrated alloys, though, cannot be determined simply by these dilute segregation energies. If one ignores interactions between the sites at the grain boundary, the above energies predict an average concentration of 48% Cu in the boundary plane for the case of the $\Sigma 5$ NiCu(10%) boundary at 800 K using the segregation expression derived for this case by McLane [156]. This is substantially smaller than the value of 74% Cu obtained in the simulation. The sense of this difference is consistent with the fact that the Ni–Cu alloy system is a clustering alloy. Thus the enhancement of the Cu concentration due to the presence of the boundary is complemented by the tendency of the Cu atoms to cluster together.

In addition to the average composition of each plane, the simulations determine the composition variations within each plane. This has been studied in detail for the case of the NiCu(10%) $\Sigma 61$ boundary. This low-angle boundary can be viewed as a square array of screw dislocations in the plane of the boundary [155]. In fig. 19, the projected atomic positions of the two planes on either side of the boundary are shown for a randomly chosen configuration from the simulation. The filled circles are Ni and the open circles are Cu atoms. The boundary clearly breaks up into regions of good match separated by a square array of poor match. These areas of poor match are the screw dislocations.

In fig. 20, the average compositions of the first three planes on one side of the boundary are shown as a function of position. The plots in fig. 20 correspond to the central unit cell of fig. 19. In particular, the screw dislocations are located along the diagonal lines that connect the midpoints of adjacent sides of this cell. For the planes two and three layers away from the boundary, the Cu concentration is highest in the center and at the corners. These regions correspond to the areas furthest away from the screw dislocations – i.e. the areas of good match between the crystals. This segregation pattern can be understood qualitatively as follows. There is a net expansion of the lattice near the boundary as discussed above. However, in the areas of good match, one would expect that the bulk lattice spacing would be

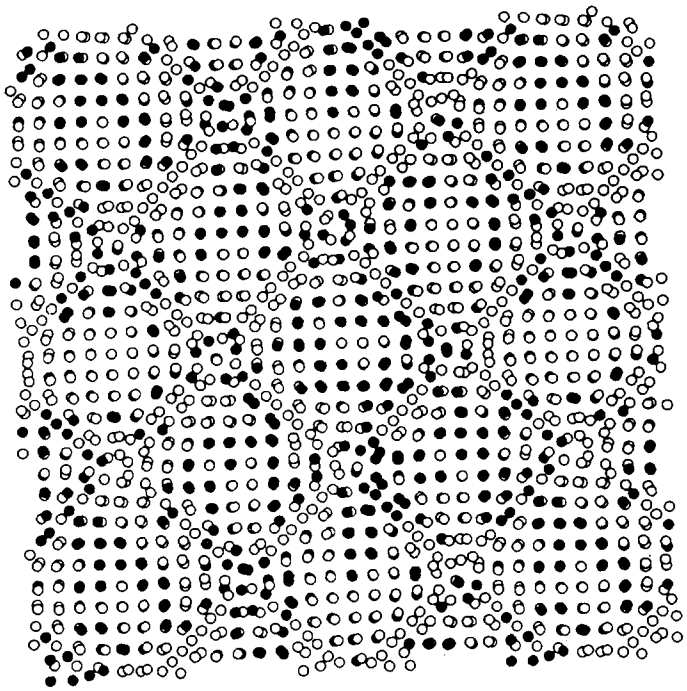

Fig. 19. Atomic positions projected onto the boundary plane for the $\Sigma 61$ twist boundary in the Ni–10 at.% Cu alloy. The first two atomic layers on either side of the boundary are shown. The open circles are Ni and the solid circles are Cu. The screw dislocation network is located in the regions of poor match between the two crystals. (From Foiles [22].)

preferred. Thus, these areas are in effect under tensile strain and Cu is enhanced in regions of tensile strain. The composition variation in the plane next to the boundary is different and more complicated. There the Cu concentration has minima at the center, corners and along the outside of the dislocations. The Cu concentration is largest at regions that are offset towards the center of the cell from the intersections of the screw dislocations.

7.4.3. Segregation to (001) twist boundaries in Pt–1 at.% Au alloys

A series of twist boundaries with θ in the range 0° to 45° [23] has been studied to determine the relationship between dislocation density and segregation. The particular values of θ chosen are 5.0°, 10.4°, 16.3°, 22.6°, 28.1°, 33.9°, 36.9°, 41.1° and 43.6°. These angles correspond to the $\Sigma = 265$, 61, 25, 13, 17, 289, 5, 73 and 29 coincident site lattice (CSL) orientations. The alloy studied is a single-phase Pt–1 at.% Au alloy in the temperature range 850–1900 K.

Fig. 21 exhibits the Au concentration for each (002) plane for Monte Carlo simulations performed at 850 K. The positions of the interface are indicated by arrows – multiple interfaces are a result of the periodic boundary conditions. This figure demonstrates that Au segregation occurs at all the twist boundaries studied; mainly the two planes that adjoin each interface are enriched in Au atoms. The segregating Au atoms sit at substitutional sites in these planes.

An average segregation enhancement factor (S_{av}) is defined to be the ratio of the solute concentration in the two planes that adjoin the interface, divided by the solute concentration

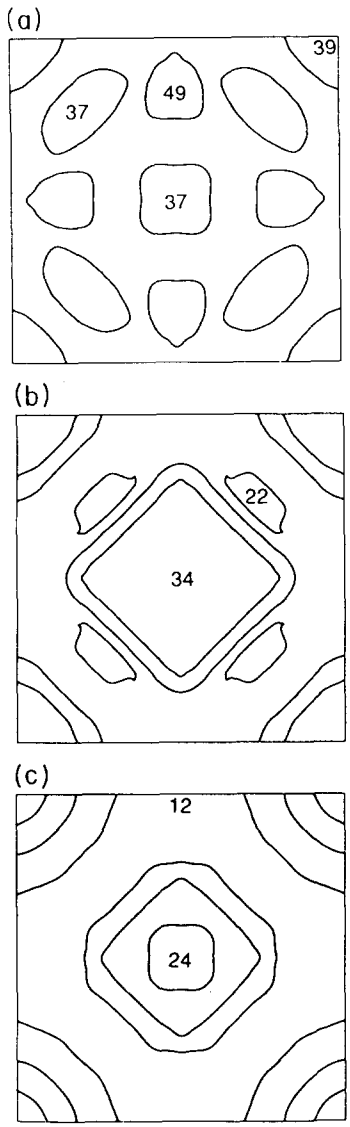

Fig. 20. Contour plots of the Cu concentration as a function of the position in the plane of the boundary for the $\Sigma 61$ twist boundary in the Ni–10 at.% Cu alloy. The first (a), second (b), and third (c) atomic layers from the boundary are shown. (From Foiles [22].)

in the bulk. Plots of S_{av} versus $\sin(\theta/2)$ at 850, 900, 1000, 1300, 1500 and 1900 K – $\sin(\theta/2)$ is proportional to the dislocation density – were calculated. At fixed temperature the value of S_{av} increases monotonically, as θ increases up to $\sin(\theta/2) \approx 0.3$, while at fixed θ the value of S_{av} decreases exponentially as temperature increases.

An Arrhenius plot of S_{av} yields straight lines for all the twist boundaries. A classical thermodynamic analysis of the Arrhenius plots yields a binding enthalpy ($\Delta h^{b}_{s\text{-}gb}$) and a binding entropy ($\Delta s^{b}_{s\text{-}gb}$) of a solute atom at a twist boundary. The range of $\Delta h^{b}_{s\text{-}gb}$ is from 0.011 ± 0.009 to 0.121 ± 0.009 eV/atom, as θ is increased from 5.0 to 36.9°. The largest value of $\Delta h^{b}_{s\text{-}gb}$ is for the $\Sigma = 5$ twist boundary. The range of $\Delta s^{b}_{s\text{-}gb}$ is from 0.07 ± 0.10 k for

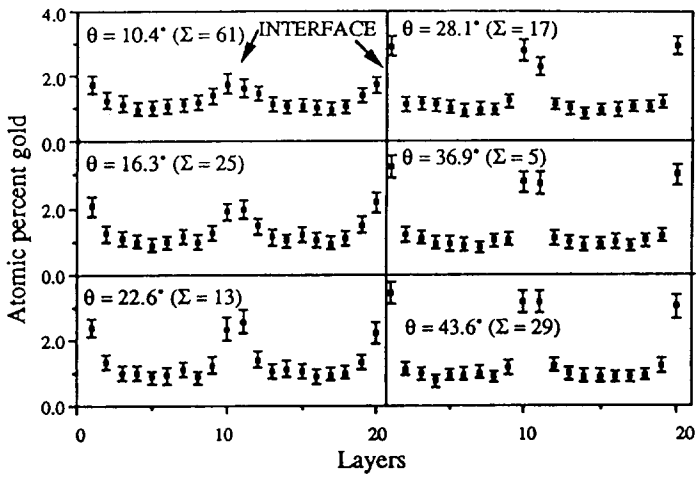

Fig. 21. The concentration of Au (at.%) in the (002) planes versus the distance normal to the interface for $\theta = 10.4°$ ($\Sigma = 61$), $\theta = 16.3°$ ($\Sigma = 25$), $\theta = 22.6°$ ($\Sigma = 13$), $\theta = 28.1°$ ($\Sigma = 17$), $\theta = 36.9°$ ($\Sigma = 9$), and $\theta = 43.6°$ ($\Sigma = 29$)[001] twist boundaries. The interfaces are indicated by arrows. There is more than one interface present because of the periodic boundary conditions employed. The concentrations are averaged over $(3–5)\times 10^6$ Monte Carlo steps and the error bars have a total length equal to four standard deviations. (From Seki et al. [23].)

$\theta = 16.3°$ to $0.46 \pm 0.09\ k$ for $\theta = 36.9°$ ($\Sigma = 5$). The values of $\Delta s^{b}_{s\text{-}gb}$ for $\theta = 5.0°$ to 16.3° are essentially the same, $0.1\ k$, when the uncertainty ($\pm 0.1\ k$) is taken into account. That all values of $\Delta s^{b}_{s\text{-}gb}$ are positive – with the exception of the 5° boundary – implies that within the context of an Einstein solid [157] the vibrational frequencies associated with a Au atom at a grain boundary are higher than those of a Au atom in the bulk. This result is qualitatively consistent with the idea that Au is an oversized substitutional atom in the cores of the dislocations.

An analysis of the two-dimensional spatial distribution of Au atoms reveals that they sit mainly in the cores of the primary grain boundary dislocations. (No evidence was found for the formation of atmospheres – due to the elastic inhomogeneity interaction – around individual screw dislocations as envisaged in the linear elasticity theory model of solute-atom segregation at dislocations [155].) These observations are the basis of a model for the Monte Carlo simulation results. We divide the grain boundary interface into two regions. The first region contains the cores of the dislocations and the second one is a region of good atomic fit. The structure of the core region is taken to be the same for all θ values studied since the $\boldsymbol{b}$ of the primary grain boundary dislocations is identical for all values of θ. The average Au concentration at an interface is the sum of the Au concentrations in the region of good atomic fit plus the concentration in the cores of the dislocations. This model leads to a linear equation for S_{av}, as a function of θ. The linear dependence holds up to $\theta \approx 35°$ since beyond this value S_{av} is approximately independent of θ; i.e. all material at the interface is at core sites, and it is not possible to increase the fraction of sites in the cores. For this model the segregation factor for the core (S_{core}) has a single value for all twist boundaries. An Arrhenius plot of S_{core} has a single value of the binding enthalpy of a Au atom to the core, 0.095 ± 0.01 eV/atom, and a single value of the binding entropy, $0.49 \pm 0.10\ k$; these values are for a core radius equal to $0.8\ |\boldsymbol{b}|$.

The physical picture that emerges from the Monte Carlo simulations is that Au segregation occurs primarily at the cores of the primary grain boundary dislocations, and therefore the Au

concentration at the interface depends on the fraction of atoms in a bicrystal that is located in the cores. This explains why the value of S_{av} is a function of θ, and why it saturates when the cores of the primary dislocations overlap. When the cores overlap all atoms at the interface are in the cores of the dislocations, and increasing θ does not significantly change the fraction of sites in the bicrystal at the cores. It is noteworthy that Wolf has shown that the energy of grain boundaries, including high-angle boundaries, can also be described in terms of a dislocation model [158].

8. Mechanical properties

This section will review the results of EAM calculations as directly related to the investigation of mechanical properties of metals. We focus on two areas of fundamental interest. The first area is the motion of dislocations in metals. We consider both free acceleration from rest and also the interaction of a dislocation with a pinning point. The second area considers the classic problem of a sharp crack in a ductile metal. Here we examine the propensity for dislocation emission as a function of loading mode, and also the effects of hydrogen on the fracture. A more detailed discussion of the results in this section may be found in Baskes and Daw [29].

8.1. Dislocations

The goal of the following calculations is to learn about dislocation motion in fcc materials and how it is affected by stress, temperature, and impurities. As a specific example we present calculations of the motion of an edge dislocation in Ni and how the dislocation interacts with small pinning points.

The boundary conditions on any present-day atomistic computer simulation prohibit us from doing an accurate simulation of a dislocation moving in an infinite medium. Generally we have used a mixture of periodic boundaries, free surfaces, and modified surfaces (see the following) and attempt to extract conclusions which are not strongly affected by these boundaries.

A typical geometry is shown in fig. 22 (see, for example, Daw et al. [27]). The size of this region is about 58 Å in the x direction, 28 Å in the y direction, and 5 Å in the z direction. This size corresponds to 706 atoms. An edge dislocation can be created by inserting two half-planes. The boundaries are periodic in the x and z directions, and the periodic lengths are held fixed during the calculation.

For some calculations, the surface in the y direction was allowed to be free. To eliminate unphysical wave motion caused by having the free surfaces in the y direction, we also experimented with another type of boundary condition, where each atom on the free surface was given an additional force (and corresponding energy) to simulate the absent bulk material. In this case, the force in a direction normal to the surface is given by $-k(y-y_0)$ where y_0 is the initial (perfect lattice) position of the atom and $k(=5.2\ \text{eV/Å}^2)$ is determined by making the second derivative of the energy with respect to displacement of an atom equal for a bulk atom and for an atom on the surface.

To initialize the calculations, the atoms are first relaxed by minimizing the energy with no applied stress at 0 K. The two half-planes (partial dislocations) separate to about 15 Å, which is near the separation expected from continuum theory.

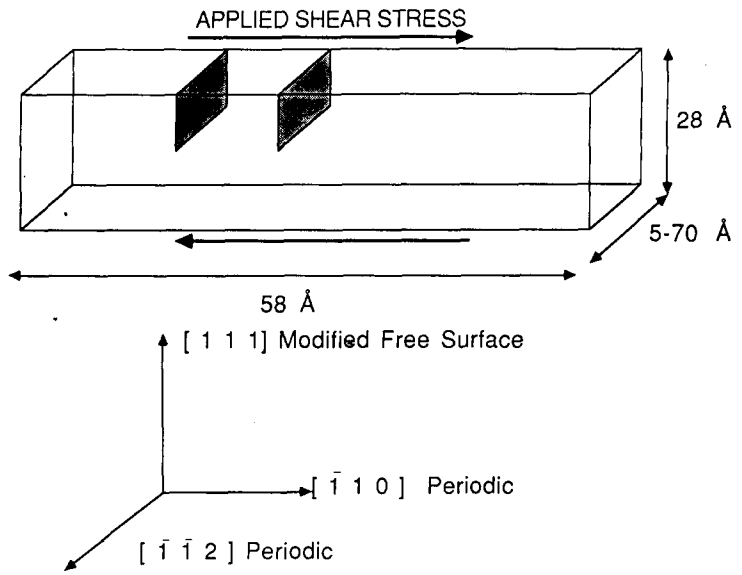

Fig. 22. The geometry which was used for some edge dislocation calculations. Two half-planes (shaded) are added to produce an edge dislocation in nickel. The boundary conditions in the x and z directions are periodic, forming an infinite array of straight dislocations. The cell is terminated by modified free surfaces in the y direction (see text for details). Approximate dimensions are shown.

To investigate the effects of stress and temperature we perform standard molecular-dynamics calculations. The temperature is attained by giving each atom an initial random velocity chosen from a Boltzmann distribution. Equipartition of kinetic and potential energy occurs in ~ 0.1 ps. The temperature is maintained by exponential relaxation at each time step (2 fs) of the average kinetic energy to the desired kinetic energy using a time constant of 0.1 ps. For example, using this method, the temperature (after the initial 0.1 ps transient) is kept to within 3 K for a desired temperature of 50 K. Similar fractional temperature deviations are found for the other temperatures considered. The stresses are introduced by applying external forces to the boundary (free surface) atoms.

We have investigated the range of stress from 15 to 60 MPa and the range of temperatures from 10 to 1000 K. Fig. 23 shows the results of calculations at 15 MPa. We show here the dislocation position as a function of time in the molecular-dynamics run. At low temperature the average position of the two partials (determined using the algorithm of Daw et al. [27]) increases smoothly to a constant velocity, but at the higher temperatures it oscillates somewhat randomly. In fact, we see in fig. 24 that, due to the strong dislocation–phonon interaction, the dislocation position at higher temperatures depends strongly on the random, initial velocities given to the atoms. We leave the higher-temperature analysis to future study and concentrate here on the runs at temperatures below 100 K where the motion is largely independent of initial random velocities.

Our results can be understood by considering the motion of a dislocation under stress in an isotropic medium [155]. From continuum theory, it can be argued that the dislocation velocity, v, is given by the following differential equation:

$$\frac{\mathrm{d}}{\mathrm{d}t}\frac{mv}{\sqrt{1-(v/c)^2}} = (\sigma-\sigma_0)b - \alpha\frac{3kT}{10b^2}\frac{v/c}{\sqrt{1-(v/c)^2}}, \tag{10}$$

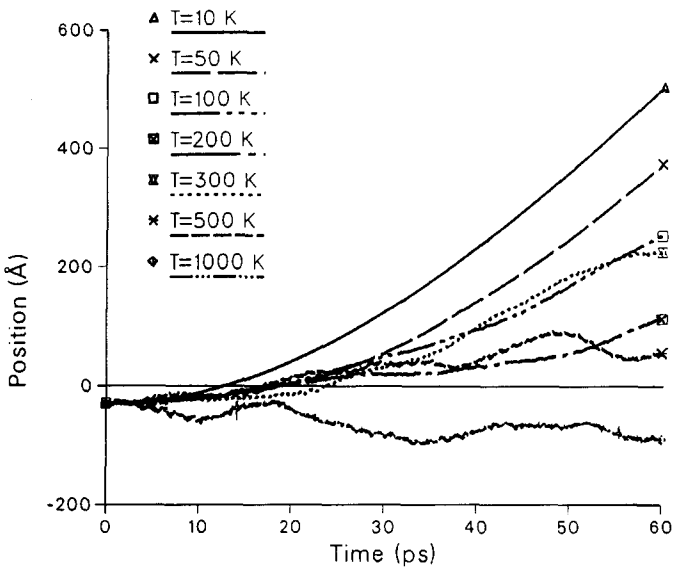

Fig. 23. Atomistic calculation of the motion of an edge dislocation in nickel. The dislocation position is given as a function of time due to an applied shear stress of 15 MPa at various temperatures, T(K). For $T \geq 100$ K, the position increases monotonically and saturates at a constant slope (velocity). At higher temperatures, the statistical fluctuations due to phonon interactions dominate the motion.

where m is the dislocation mass per unit length, c is a limiting velocity, σ is the applied stress, σ_0 a friction stress, b the Burgers vector of the dislocation, and α is a dimensionless constant. The left-hand side is simply the time rate of change of the dislocation momentum. The first term on the right-hand side is the driving force for motion; the second term is due to

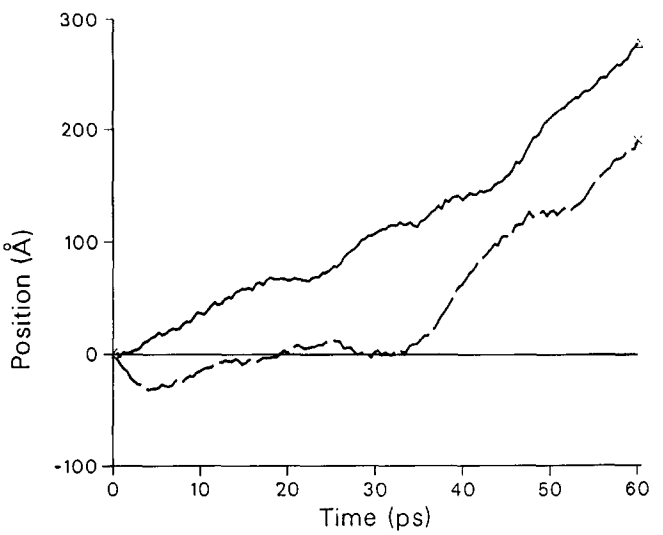

Fig. 24. Dislocation motion depends upon thermal fluctuations. The position of an edge dislocation in nickel is plotted as a function of time for an applied shear stress of 60 MPa at a temperature of 500 K. Shown are two trajectories for different initial random velocities. The variation in behavior is due to the large phonon–dislocation interaction at high temperature.

Table 17
Dislocation-dynamics constants for Ni

c (Å/ps)	20
m (atoms/Burgers distance)	0.2
α	0.98
σ_0 (MPa)	4

the dislocation–phonon drag which limits the dislocation motion. We have added a scaling factor, α, and a saturation factor to the classical expression by Leibfried [159] to facilitate comparison with the atomistic calculations. We may solve the equation of motion analytically for the dislocation velocity and then numerically for the dislocation position in terms of four unknown material constants m, c, α, and σ_0. By fitting these constants to the atomistic data, we obtain both a confirmation of the validity of the form of the continuum model and the values of the material constants. The results of this fit are given in table 17.

The limiting velocity of 20 Å/ps is quite close to the lower transverse velocity (23 Å/ps) in the coordinate system used here. (These results are for the "modified" surface boundary conditions; for a free surface in the y direction, the limiting velocity is somewhat less, consistent with what one expects from a finite slab [27].) The values of the dislocation mass and friction stress appear quite reasonable while the scaling factor for the drag term is amazingly close to unity. The fit, while not perfect, certainly shows that the continuum model contains the correct basic physics of dislocation motion.

We now proceed to investigate the interaction of dislocations with obstacles. In order to perform these calculations, we use the same geometry as in fig. 22, but increase the z dimension of our region to simulate experimentally observed obstacle separations. As a first example we remove an atom on the dislocation slip plane and its 12 neighbors, creating a 13-atom void ($\sim$ 6.4 Å diameter). We now apply a shear stress and observe the dislocation motion. The results at 300 K are shown in fig. 25 where we see that at a stress of 90 MPa ($\sim$ 1.5 times the experimental yield stress of pure annealed nickel), these small voids separated by 35 Å provide a barrier for dislocation motion. At a stress of 120 MPa, the dislocation is able to penetrate this barrier.

We now place 19 He atoms in the void and repeat the calculations. This ratio of 19 He/13 V is representative of the ratio found in samples which have undergone prolonged exposure to tritium. The results of the pinning stress are shown in fig. 26 as a function of inverse defect spacing. Here the error bars on the symbols denote the stress range where we go from pinning to not pinning. We expect a linear relationship from continuum models. Note that as we would expect, the $He_{19}V_{13}$ is more of an obstacle to dislocation motion than the V_{13}, and second that the pinning stress varies linearly with the inverse defect spacing. Also shown in fig. 26 are the results of calculations of a $He_{19}V_{13}$ bubble with the 13 nickel atoms (from the void) placed in a loop around the bubble. This configuration is representative of the expected arrangement that would occur from the self-trapping of helium where the punched-out nickel atoms would remain trapped to the small bubble. The pinning stress for this configuration is extremely high (900 MPa). We find that as the dislocation moves past this obstacle, it "collects" the interstitial atoms, leaving the bubble without a loop and the dislocation with a segment that has climbed. We see this effect in the atomistic calculations where the 13 atoms from the loop appear along part of the dislocation line and the loop disappears from around the bubble. Of course, it is not the same 13 nickel atoms moving along with the dislocation

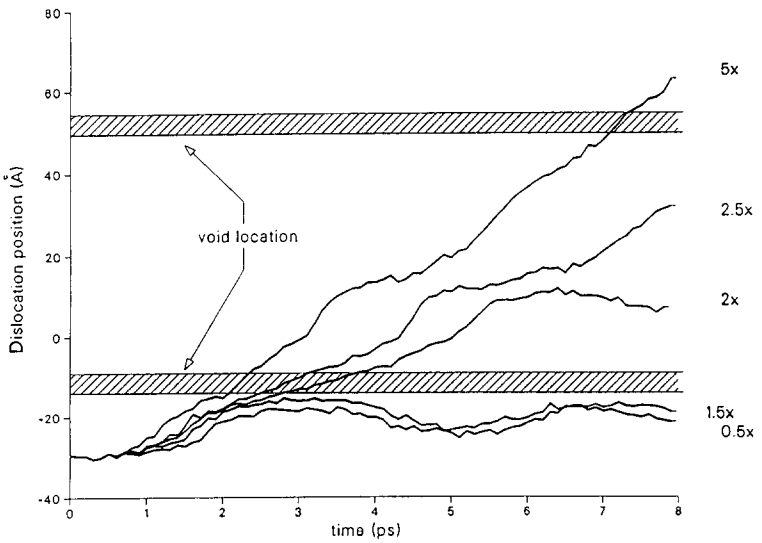

Fig. 25. Effect of a small void on dislocation motion. The dislocation position versus time is plotted for the case of interaction with an array of small vacancy clusters (V_{13}) separated by 35 Å along the dislocation core at 300 K. The voids are present every 60 Å in the direction of motion of the dislocation as indicated in the figure. The stress for each curve is indicated as a multiple of the yield stress of annealed Ni (60 MPa). For stresses ≤ 90 MPa, the dislocation is pinned. At higher stress levels the dislocation passes the voids, but is clearly affected by them.

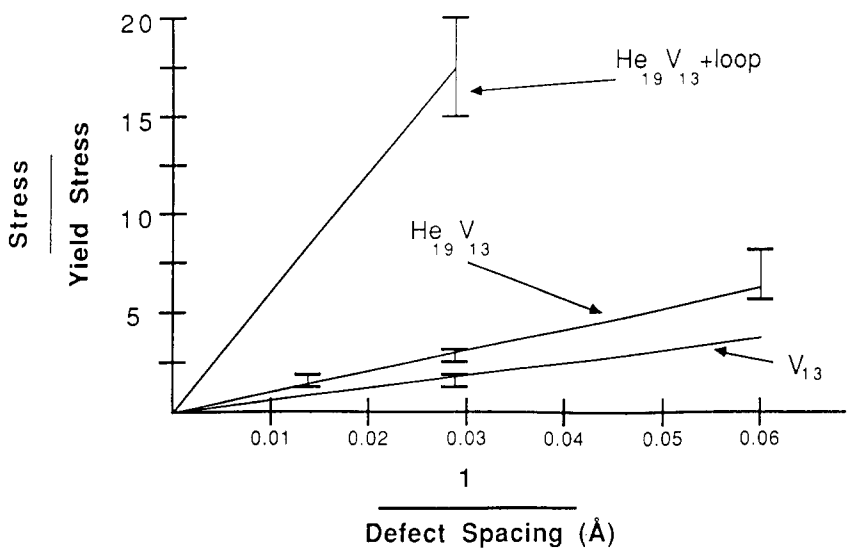

Fig. 26. Effect of defect character on obstacle strength. The critical stress for dislocation pinning versus inverse defect spacing along the dislocation core is shown. The stress is scaled by the yield stress in annealed nickel (60 MPa). The lower stress level of each error bar indicates the maximum stress where pinning occurs while the upper level indicates the minimum stress where lack of pinning is observed. Shown in the figure are three cases, a small void (V_{13}), a small helium bubble ($He_{19}V_{13}$), and a small bubble with an attached dislocation loop.

that were originally in the loop. The loop atoms simply take normal lattice positions as the dislocation moves away from the He bubble. It is interesting to note that in contrast to this effect, the dislocation does not "collect" either vacancies from the void or helium atoms from the bubble. In both of these cases the defect remains intact.

8.2. *Fracture*

In this section, we discuss the effects of loading mode on the details of fracture at an atomistic crack tip. First we consider these effects in pure nickel and then contrast the behavior with stoichiometric nickel hydride. Other detailed work on the nature of fracture using the EAM has been carried out [31,32] and the interested worker is referred to those papers.

The geometry we use is shown in fig. 27. The initial atom positions are determined by displacement of a perfect lattice using the continuum anisotropic theory of Sih and Liebowitz [160]. The origin of the continuum crack was chosen exactly between two planes of atoms in both the x and y directions. A small number of calculations showed that the choice of origin was of little importance. The elastic constants used in determining the continuum displacements were those of the atomistic model.

The calculations were performed by relaxing the atoms at 0 K in region I while holding the atoms in region II fixed at their positions given by continuum theory. Region I consists of $\sim$ 1700 atoms ($\sim$ 35 Å diameter) while region II is a shell of 12 Å thickness, large enough to include all interactions of region I atoms. A few calculations were performed to investigate the effect of the size of the regions. Increasing the size to 40 Å in region I did not affect the fracture mode for the cases tested.

The calculations for Ni are summarized in fig. 28a. Four different events occurred at the crack tip depending on the K_I and K_{II} (stress intensity factors [161]): crack closure; brittle fracture; ductile fracture; and slip along the crack plane. The most obvious result is that for small values of K_I and K_{II} the crack healed itself. We were able to ascertain crack tip closure by looking at the relative displacement of the atoms near the crack tip. These atoms moved from their initial positions determined from continuum theory toward the free volume of the crack. Opposite to this behavior, we find for strictly K_I loading above a critical value, motion of these atoms directly away from the open space of the crack. This mode of failure we call

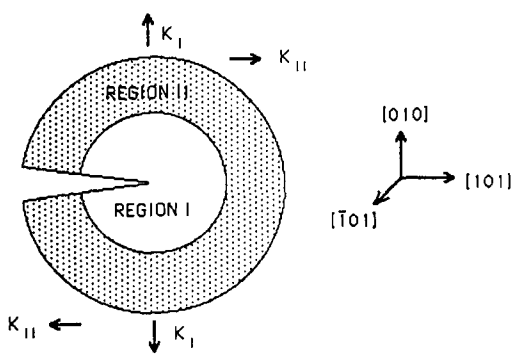

Fig. 27. Geometry for the loading-mode calculations. Atoms in region I are movable while atoms in region II are fixed. Initial atom positions are taken from anisotropic continuum theory for applied loading conditions K_I (tensile) and K_{II} (shear).

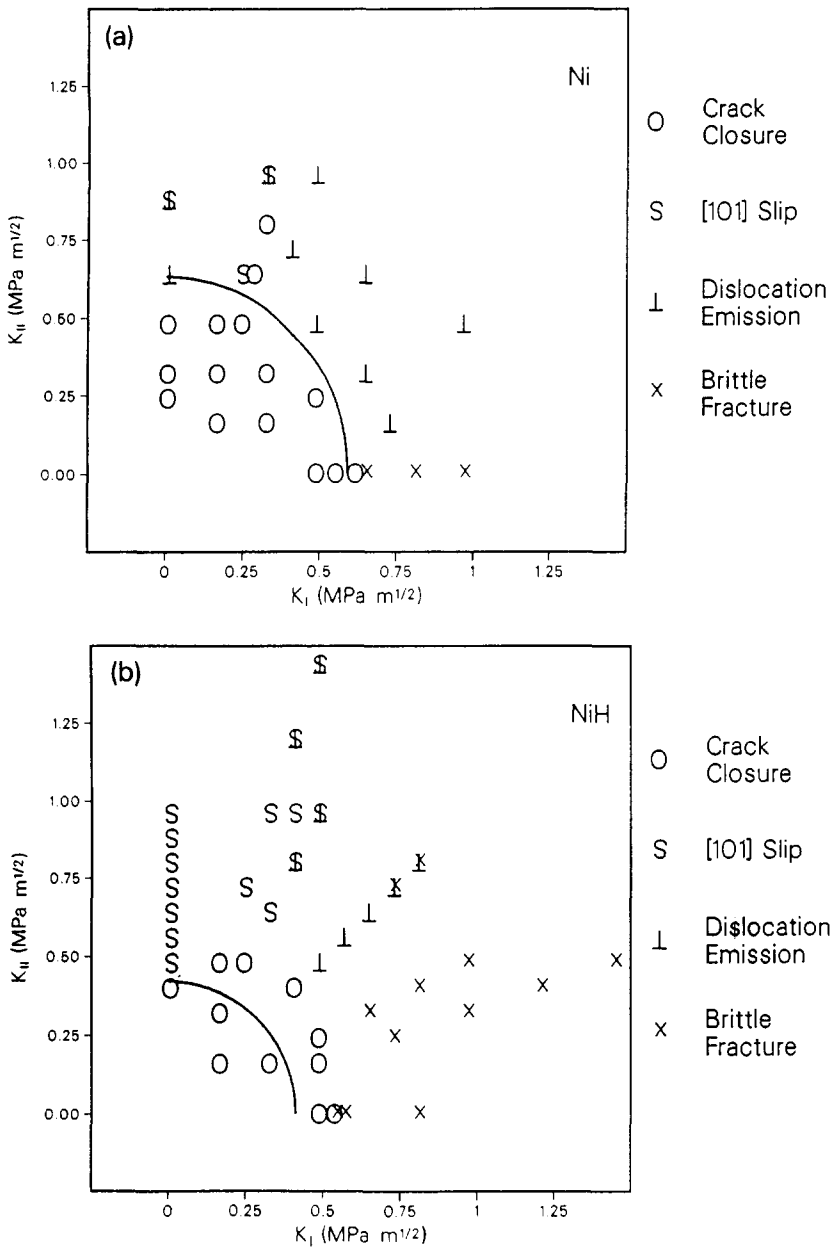

Fig. 28. Crack-tip response to loading mode, for (a) Ni and (b) NiH. The two loading modes are I (tensile) and II (shear). The response to various mixed loading conditions is of four types: crack closure, [101] slip, dislocation emission, and brittle fracture. It is seen that nickel is much more ductile than NiH and the addition of mode II loading enhances ductility in both materials. The solid curve denotes the Griffith condition.

brittle fracture as it represents a simple separation of the crack planes. The third event and most common mode of failure is a ductile mode characterized by motion of atoms in the $[\bar{1}2\bar{1}]$ direction in the $(1\bar{1}1)$ plane. This motion represents the emission of a partial dislocation and the concomitant blunting of the crack tip. Our region was not large enough to see the

Table 18
Energy factors and surface energies for Ni and NiH

	Ni	NiH
A_I (Å^3/eV)	0.674	0.734
A_{II} (Å^3/eV)	0.584	0.692
γ_{100} (erg/cm^2)	732	387

emission of the second partial dislocation; the back stress of the fixed region II opposes this emission. The fourth event occurs with predominantly mode II loading and represents slip along the crack plane in the [101] direction. This mode is sometimes seen in combination with the partial dislocation emission. We note (fig. 28a) that as expected, the failure in Ni is predominantly ductile with dislocation emission and slip occurring over most of the K_I/K_{II} space.

In contrast to these results for pure Ni we see in fig. 28b for fully stoichiometric NiH that over a large range of (K_I, K_{II}) the fracture mode is brittle. Also the [101] slip regime is extended as the dislocation emission regime is decreased. A general conclusion for both Ni and NiH is that as the amount of mode II loading increases, the failure mode goes from brittle to dislocation emission to slip.

We can compare our atomistic results to the Griffith criterion. For an anisotropic material the total energy rate, G, is given by

$$G = A_I K_I^2 + A_{II} K_{II}^2, \tag{11}$$

where A_I, A_{II} are dependent on material properties and crack orientation. For our case the values of A_I, A_{II} are given in table 18.

The Griffith condition for brittle fracture is that the total energy rate, G, be equal to two times the surface energy, in our case γ_{100}. This criterion is also shown in fig. 28 as the full line. The surface energies used in fig. 28 are those predicted by the EAM for Ni and NiH (table 18). The value we predict for Ni is considerably lower than the measured value for polycrystalline nickel of over 2000 erg/cm^2. We expect a (100) surface to be lower than polycrystalline, but not this low. This disagreement, which was discussed in section 6.1, would lead to a consistent underestimate of the Griffith K.

We note that in Ni for pure mode I loading the Griffith criterion divides the region of crack closure exactly. What is even more interesting is that this condition seems to work quite well even as mode II loading is added and the failure becomes ductile. In no case is there failure with (K_I, K_{II}) less than the Griffith criterion. A similar conclusion may be drawn for NiH, but in this case the Griffith criterion is somewhat more conservative.

9. Summary

The embedded-atom method is a semi-empirical method for performing calculations of defects in metals. The EAM incorporates a picture of metallic bonding, for which there is some fundamental basis. The limitations of the EAM are fairly well characterized: it works best for purely metallic systems with no directional bonding; it does not treat covalency or significant charge transfer; and it does not handle Fermi-surface effects. The main physical

property incorporated in the EAM is the moderation of bond strength by other bonds (coordination-dependent bond strength). Within these constraints, the EAM provides a very useful and robust means of calculating approximate structure and energetics, from which many interesting properties of metals can be obtained.

We believe that atomistic calculations will continue to play an important role in the development of materials theory. Where the EAM can be useful, there is a tremendous number of interesting projects that have yet to be carried out. The understanding of mechanical properties on an atomistic level has only just begun. For materials where the EAM is not expected to work well, there are recent developments which may allow calculations similar to those presented here. We have mentioned already the problem of treating directional bonding in semiconductors and elements from the transition series. One approach which promises to be useful for treating directional bonding is reviewed by Carlsson [70]; the interested reader is encouraged to start there.

Acknowledgements

The authors would like to acknowledge that many of the applications of the EAM covered in this review were done in collaboration with several very capable colleagues. Collaborators have included Dr. E.C. Sowa (now at Lawrence Livermore National Laboratory), Dr. J.S. Nelson (now at Sandia National Laboratories in New Mexico), Professor J.B. Adams (now at University of Illinois), and Dr. Alan Wright (now at Sandia in California). This work was supported by the U.S. Department of Energy, Office of Basic Energy Sciences, Division of Materials Science.

References

[1] M.S. Daw and M.I. Baskes, Phys. Rev. Letters 50 (1983) 1285.
[2] M.S. Daw and M.I. Baskes, Phys. Rev. B 29 (1984) 6443.
[3] S.M. Foiles, M.I. Baskes and M.S. Daw, Phys. Rev. B 33 (1986) 7983.
[4] S.M. Foiles, M.I. Baskes and M.S. Daw, Phys. Rev. B 37 (1988) 10387.
[5] M.S. Daw, Phys. Rev. B 39 (1989) 7441.
[6] V. Heine and J. Hafner, in: Many-Atom Interactions in Solids, eds. M.J. Puska, R.M. Nieminen and M. Manninen (Springer, Berlin, 1990).
[7] G. Jacucci, in: Diffusion in Crystalline Solids, eds. G.E. Murch and A.S. Nowick (Academic Press, New York, 1984).
[8] A.J.C. Ladd and L.V. Woodcock, Mol. Phys. 36 (1978) 611.
[9] F. Ercolessi, M. Parrinello and E. Tosatti, Phil. Mag. A 58 (1988) 213.
[10] M.S. Daw and R.D. Hatcher, Solid State Commun. 56 (1985) 697.
[11] S.M. Foiles and M.S. Daw, Phys. Rev. B 38 (1988) 12643.
[12] S.M. Foiles and J.B. Adams, Phys. Rev. B 40 (1989) 5909.
[13] S.M. Foiles, Phys. Rev. B 32 (1985) 3409.
[14] S.M. Foiles, M.I. Baskes and M.S. Daw, in: Interfacial Structure, Properties and Design, eds. M.H. Yoo, W.A.T. Clark and C.L. Briant (Materials Research Society, Pittsburgh, PA, 1988).
[15] S.M. Foiles, Acta Metall. 37 (1989) 2815.
[16] M.J. Mills, G.J. Thomas, M.S. Daw and F. Cosandey, Mater. Res. Soc. Symp. Proc. 159 (1989) 365.
[17] U. Dahmen, C.J.D. Hetherington, M.A. O'Keefe, K.H. Westmacott, M.J. Mills, M.S. Daw and V. Vitek, Phil. Mag. Letters 62 (1990) 327.
[18] M.J. Mills and M.S. Daw, Mater. Res. Soc. Symp. Proc. 183 (1990) 15.
[19] M.J. Mills, M.S. Daw, G.J. Thomas and F. Cosandey, Ultramicroscopy 40 (1992) 247.
[20] S.M. Foiles and M.S. Daw, J. Met. 39 (1987) 39.

[21] S.M. Foiles, in: High-Temperature Ordered Intermetallic Alloys, Vol. 2, eds. N.S. Stoloff, C.C. Koch, C.T. Liu and O. Izumi (Materials Research Society, Pittsburgh, PA, 1987).
[22] S.M. Foiles, Phys. Rev. B 40 (1989) 11502.
[23] A. Seki, D.N. Seidman, Y. Oh and S.M. Foiles, Acta Metall. 39 (1991) 3167.
[24] J.B. Adams, S.M. Foiles and W.G. Wolfer, J. Mater. Res. 4 (1989) 102.
[25] J.B. Adams, S.M. Foiles and W.G. Wolfer, in: Atomistic Simulation of Materials, eds. D. Srolovitz and V. Vitek (Plenum Press, New York, 1989).
[26] M.I. Baskes, S.M. Foiles and M.S. Daw, J. Phys. (Paris) C5 (1988) 483.
[27] M.S. Daw, M.I. Baskes, C.L. Bisson and W.G. Wolfer, in: Modelling Environmental Effects on Crack Growth Processes, Metallurgical Society Fall Meeting, Toronto, Canada (1985), eds. R.H. Jones and W.W. Gerberich.
[28] M.S. Daw and M.I. Baskes, in: NATO Advanced Workshop on Physics and Chemistry of Fracture, Bad Reichenhall, West Germany, eds. R.M. Latanision and R.H. Jones (Nijhoff, Dordrecht, 1986).
[29] M.I. Baskes and M.S. Daw, in: Fourth International Conference on the Effect of Hydrogen on the Behavior of Materials, Jackson Lake Lodge, Moran, WY, eds. N. Moody and A. Thompson (The Minerals, Metals, and Materials Society, Warrendale, PA, 1989).
[30] R.G. Hoagland, M.I. Baskes, M.S. Daw and S.M. Foiles, J. Mater. Res. 5 (1990) 313.
[31] R.G. Hoagland, M.S. Daw, S.M. Foiles and M.I. Baskes, in: Atomic Scale Calculations of Structure in Materials, eds. M.S. Daw and M.A. Schlüter (Materials Research Society, Pittsburgh, PA, 1990).
[32] R.G. Hoagland, M.S. Daw and J.P. Hirth, J. Mater. Res. 6 (1991) 2565.
[33] S.M. Foiles, Surface Sci. 191 (1987) L779.
[34] M.S. Daw and S.M. Foiles, Phys. Rev. Letters 59 (1987) 2756.
[35] M.S. Daw and S.M. Foiles, in: 2nd International Conference on the Structure of Surfaces, Amsterdam, The Netherlands, eds. J.F. van der Veen and M.A. van Hove (Springer, Berlin, 1987).
[36] M.S. Daw and S.M. Foiles, J. Vacuum Sci. Technol. A 4 (1986) 1412.
[37] S.M. Foiles and M.S. Daw, J. Vacuum Sci. Technol. A 3 (1985) 1565.
[38] M.S. Daw and S.M. Foiles, in: 1st International Conference on the Structure of Surfaces, Berkeley, CA, eds. M.A. van Hove and S.Y. Tong (Springer, Berlin, 1985).
[39] T.E. Felter, S.M. Foiles, M.S. Daw and R.H. Stulen, Surface Sci. 171 (1986) L379.
[40] M.S. Daw and S.M. Foiles, Phys. Rev. B 35 (1987) 2128.
[41] T.L. Einstein, M.S. Daw and S.M. Foiles, Surface Sci. 227 (1990) 114.
[42] S.M. Foiles, Phys. Rev. B 32 (1985) 7685.
[43] S.M. Foiles, J. Vacuum Sci. Technol. A 4 (1986) 761.
[44] S.M. Foiles, in: Computer-Based Microscopic Description of the Structure and Properties of Materials, eds. J. Broughton, W. Krakow and S.T. Pantelides (Materials Research Society, Pittsburgh, PA, 1986).
[45] S.M. Foiles, in: Physical and Chemical Properties of Thin Metal Overlayers and Alloy Surfaces, eds. D.M. Zehner and D.W. Goodman (Materials Research Society, Pittsburgh, PA, 1987).
[46] S.M. Foiles, J. Vacuum Sci. Technol. A 5 (1987) 889.
[47] S.M. Foiles, Surface Sci. 191 (1987) 329.
[48] S.M. Foiles, in: Surface Segregation and Related Phenomena, eds. P.A. Dowben and A. Miller (CRC Press, Boca Rotan, 1990).
[49] J.S. Nelson, M.S. Daw and E.C. Sowa, Phys. Rev. B 40 (1989) 1465.
[50] J.S. Nelson, E.C. Sowa and M.S. Daw, Phys. Rev. Letters 61 (1988) 1977.
[51] P. Schwoebel, S.M. Foiles and G. Kellogg, Phys. Rev. B 40 (1989) 10639.
[52] A.F. Wright, M.S. Daw and C.Y. Fong, Phys. Rev. B 42 (1990) 9409.
[53] J.K. Nørskov and N.D. Lang, Phys. Rev. B 21 (1980) 2131.
[54] J.K. Nørskov, Phys. Rev. B 26 (1982) 2875.
[55] K.W. Jacobsen, J.K. Nørskov and M.J. Puska, Phys. Rev. B 35 (1987) 7423.
[56] K.W. Jacobsen, in: Many-Atom Interactions in Solids, eds. M.J. Puska, R.M. Nieminen and M. Manninen (Springer, Berlin, 1990).
[57] P. Stoltze, J.K. Nørskov and U. Landman, Surface Sci. 220 (1989) L693.
[58] K.W. Jacobsen and J.K. Nørskov, in: The Structure of Surfaces, Vol. 2, eds. J.F. van der Veen and M.A. van Hove (Springer, Berlin, 1988).
[59] K.W. Jacobsen and J.K. Nørskov, Phys. Rev. Letters 59 (1987) 2764.
[60] K.W. Jacobsen and J.K. Nørskov, Phys. Rev. Letters 60 (1988) 2496.
[61] K.W. Jacobsen and J.K. Nørskov, preprint (1989).
[62] S. Myllyrinne, M. Manninen and J.K. Nørskov, in: Many-Atom Interactions in Solids, eds. M.J. Puska, R.M. Nieminen and M. Manninen (Springer, Berlin, 1990).

[63] J.D. Kress and A.E. DePristo, J. Chem. Phys. 87 (1987) 4700.
[64] J.D. Kress and A.E. DePristo, J. Chem. Phys. 88 (1988) 2596.
[65] J.D. Kress, M.S. Stave and A.E. DePristo, J. Phys. Chem. 93 (1989) 1556.
[66] T.J. Raeker and A.E. DePristo, Phys. Rev. B 39 (1989) 9967.
[67] T.J. Raeker and A.E. DePristo, Intern. Rev. Phys. Chem. 10 (1991) 1.
[68] S.B. Sinnott, M.S. Stave, T.J. Raeker and A.E. DePristo, Phys. Rev. B 44 (1991) 8927.
[69] M.S. Stave, D.E. Sanders, T.J. Raeker and A.E. DePristo, J. Chem. Phys. 93 (1990) 4413.
[70] A. Carlsson, in: Solid State Physics, Vol. 43, eds. H. Ehrenreich and D. Turnbull (Academic Press, New York, 1990).
[71] J. Friedel, Phil. Mag. 43 (1952) 153.
[72] M.J. Puska, R.M. Nieminen and M. Manninen, Phys. Rev. B 24 (1980) 3037.
[73] M.J. Stott and E. Zaremba, Phys. Rev. B 22 (1980) 1564.
[74] P. Nordlander, S. Holloway and J.K. Nørskov, Surface Sci. 136 (1984) 59.
[75] M. Manninen, Phys. Rev. B 34 (1986) 8486.
[76] M.W. Finnis and J.E. Sinclair, Phil. Mag. A 50 (1984) 45.
[77] S.P. Chen, A. Voter and D.L. Srolovitz, Phys. Rev. Letters 57 (1986) 1308.
[78] F. Ercolessi, E. Tosatti and M. Parrinello, Surface Sci. 177 (1986) 314.
[79] F. Ercolessi, E. Tosatti and M. Parrinello, Phys. Rev. Letters 57 (1986) 719.
[80] J.R. Smith and A. Banerjea, Phys. Rev. B 37 (1988) 10411.
[81] J.R. Smith and A. Banerjea, Phys. Rev. Letters 59 (1987) 2451.
[82] P. Hohenberg and W. Kohn, Phys. Rev. B 136 (1964) 864.
[83] J.H. Rose, J.R. Smith, F. Guinea and J. Ferrante, Phys. Rev. B 29 (1984) 2963.
[84] S.M. Foiles and M.S. Daw, J. Mater. Res. 2 (1987) 5.
[85] R.A. Johnson, Phys. Rev. B 37 (1988) 6121.
[86] R.A. Johnson, Phys. Rev. B 37 (1988) 3924.
[87] A.A. Maradudin, E.W. Montroll, G.H. Weiss and I.P. Ipatova, in: Solid State Physics, Suppl. 3. Theory of Lattice Dynamics in the Harmonic Approximation, 2nd Ed., eds. H. Ehrenreich, F. Seitz and D. Turnbull (Academic Press, New York, 1971).
[88] E.C. Svensson, B.N. Brockhouse and J.M. Rowe, Phys. Rev. 155 (1967) 619.
[89] N. Luo, W. Xu and S.C. Shen, Solid State Commun. 69 (1989) 155.
[90] N. Luo, W. Xu and S.C. Shen, Phys. Stat. Sol. 147b (1988) 511.
[91] Y. Waseda and M. Ohtani, Phys. Stat. Sol. 62b (1974) 535.
[92] M. Marchese, G. Jacucci and C.P. Flynn, Phil. Mag. Letters 57 (1988) 25.
[93] K.A. Gschneidner Jr., in: Solid State Physics, Vol. 16, eds. F. Seitz and D. Turnbull (Academic Press, New York, 1964).
[94] R. Hultgren, P.D. Desai, D.T. Hawkins, M. Gleiser, K.K. Kelley and D.D. Wagman, Selected Values of the Thermodynamic Properties of the Elements (American Society for Metals, Metals Park, OH, 1973).
[95] S.M. Foiles, M.I. Baskes and M.S. Daw, Phys. Rev. B 37 (1988) 10378.
[96] A.D. LeClaire, J. Nucl. Mater. 69/70 (1978) 70.
[97] M.R. Fitzsimmons and S.L. Sass, Acta Metall. 37 (1989) 1009.
[98] I. Majid, P.D. Bristowe and R.W. Balluffi, Phys. Rev. 40 (1989) 2779.
[99] K.L. Merkle, J. Phys. (Paris) 51 C1 (1990) 251.
[100] F. Cosandey, S.-W. Chan and P. Stadlemann, J. Phys. (Paris) 51 C1 (1990) 109.
[101] D. Wolf and J. Lutsko, Phys. Rev. Letters 60 (1988) 1170.
[102] D. Wolf, J. Lutsko and M. Kluge, in: Atomistic Simulations of Materials – Beyond Pair Potentials, eds. V. Vitek and D.J. Srolovitz (Plenum Press, New York, 1988).
[103] J.B. Adams, W.G. Wolfer and S.M. Foiles, Phys. Rev. B 40 (1989) 9479.
[104] S.M. Foiles, in: Atomic Scale Calculations of Structure in Materials, eds. M.S. Daw and M.A. Schlüter (Materials Research Society, Pittsburgh, PA, 1990).
[105] J.D. Weeks, in: Ordering in Strongly Fluctuating Condensed Matter Systems, ed. T. Riste (Plenum Press, New York, 1980).
[106] W.R. Tyson and W.A. Miller, Surface Sci. 62 (1977) 267.
[107] A.F. Voter and S.P. Chen, Mater. Res. Soc. Symp. Proc. 82 (1987) 175.
[108] S.P. Chen, D.J. Srolovitz and A.F. Voter, J. Mater. Res. 4 (1989) 62.
[109] T. Ning, Q. Yu and Y. Ye, Surface Sci. 206 (1988) L857.
[110] M. Wuttig, R. Franchy and H. Ibach, Solid State Commun. 57 (1986) 445.
[111] M. Wuttig, R. Franchy and H. Ibach, Z. Physik B 65 (1986) 71.

[112] G. Santoro, A. Franchini, V. Bortolani, U. Harten, J.P. Toennies and C. Wöll, Surface Sci. 183 (1987) 180.
[113] V. Bortolani, A. Franchini, F. Nizzoli and G. Santoro, Phys. Rev. Letters 52 (1984) 429.
[114] V. Bortolani, G. Santoro, U. Harten and J.P. Toennies, Surface Sci. 148 (1984) 82.
[115] V. Bortolani, A. Franchini, F. Nizzoli and G. Santoro, Surface Sci. 152 (1985) 811.
[116] M.H. Mohamed, L.L. Kesmodel, B.M. Hall and D.L. Mills, Phys. Rev. B 37 (1988) 2763.
[117] B.M. Hall, D.L. Mills, M.H. Mohamed and L.L. Kesmodel, Phys. Rev. B 38 (1988) 5856.
[118] N. Luo, W. Xu and S.C. Shen, Solid State Commun. 67 (1988) 837.
[119] A.A. Maradudin, R.F. Wallis, A.R. McGurn, M.S. Daw and A.J.C. Ladd, in: Lattice Dynamics and Semiconductor Physics (World Scientific, Singapore, 1990).
[120] L. Yang, T.S. Rahman and M.S. Daw, Phys. Rev. B 44 (1991) 13725.
[121] P. Nordlander and S. Holmstrom, Surface Sci. 149 (1985) 443.
[122] A.G. Eguiluz, D.A. Campbell, A.A. Maradudin and R.F. Wallis, Phys. Rev. B 30 (1984) 5449.
[123 J.-P. Muscat, Phys. Rev. B 33 (1986) 8136.
[124] T.L. Einstein and J.R. Schrieffer, Phys. Rev. B 7 (1973) 3629.
[125] K. Christmann, R.J. Behm, G. Ertl, M.A. van Hove and W.H. Weinberg, J. Chem. Phys. 70 (1979) 4168.
[126] R.J. Behm, K. Christmann and G. Ertl, Surface Sci. 99 (1980) 320.
[127] J.C. Campuzano, A.M. Lahee and G. Jennings, Surface Sci. 152/153 (1985) 68.
[128] J.-K. Zuo, Y.-L. He, G.-C. Wang and T.E. Felter, J. Vacuum Sci. Technol. A 8 (1990) 2474.
[129] M. Garofalo, E. Tosatti and F. Ercolessi, Surface Sci. 188 (1987) 321.
[130] W. Moritz and D. Wolf, Surface Sci. 88 (1979) L29.
[131] G. Binnig, H. Rohrer, C. Gerber and E. Weibel, Surface Sci. 131 (1983) L379.
[132] W. Moritz and D. Wolf, Surface Sci. 163 (1985) L655.
[133] M. Copel and T. Gustafsson, Phys. Rev. Letters 57 (1986) 723.
[134] E.C. Sowa, M.A. van Hove and D.L. Adams, Surface Sci. 199 (1988) 174.
[135] P. Fenter and T. Gustafsson, Phys. Rev. B 38 (1988) 10197.
[136] J.C. Hamilton, Phys. Rev. Letters 42 (1979) 989.
[137] P. Wynblatt and R.C. Ku, in: Interfacial Segregation, eds. W.C. Johnson and J.M. Blakely (American Society for Metals, Metals Park, OH, 1979).
[138] A.D. van Langeveld, H.A.C.M. Hendrickx and B.E. Nieuwenhuys, Thin Solid Films 109 (1983) 179.
[139] W.F. Egelhoff Jr., Phys. Rev. B 30 (1984) 1052.
[140] Y.S. Ng, T.T. Tsong and S.B. McLane, Phys. Rev. Letters 42 (1979) 588.
[141] P.R. Webber, C.E. Rojas, P.J. Dobson and D. Chadwick, Surface Sci. 105 (1981) 20.
[142] H.H. Brongersma, M.J. Sparnaay and T.M. Buck, Surface Sci. 71 (1978) 657.
[143] H.H. Brongersma, P.A.J. Ackermans and A.D. van Langeveld, Phys. Rev. B 34 (1986) 5974.
[144] T. Sakurai, T. Hashizume, A. Jimbo, A. Sakai and S. Hyodo, Phys. Rev. Letters 55 (1985) 514.
[145] G.A. Kok, A. Noordermeer and B.E. Nieuwenhuys, Surface Sci. 152 (1985) 505.
[146] A. Noordermeer, G.A. Kok and B.E. Nieuwenhuys, Surface Sci. 165 (1986) 375.
[147] D.G. Swartzfager, S.B. Ziemecki and M.J. Kelly, J. Vacuum Sci. Technol. 19 (1981) 185.
[148] G. Hetzendorf and P. Varga, Nucl. Instr. Methods B 18 (1987) 501.
[149] P.W. Palmberg and T.N. Rhodin, J. Chem. Phys. 49 (1968) 134.
[150] G.W. Graham, Surface Sci. 184 (1987) 137.
[151] Z.Q. Wang, Y.S. Li, C.K.C. Lok, J. Quinn, F. Jona and P. Marcus, Solid State Commun. 62 (1987) 181.
[152] A.H. King and M.H. Yoo, Scripta Metall. 21 (1987) 1115.
[153] R.A.D. Mackenzie and S.L. Sass, Scripta Metall. 22 (1988) 1807.
[154] M.J. Mills, Scripta Metall. 23 (1989) 2061.
[155] J.P. Hirth and J. Lothe, Theory of Dislocations (Wiley, New York, 1982).
[156] D. McLane, Grain Boundaries in Metals (Clarendon, Oxford, 1957).
[157] H.B. Huntington, G.A. Shirn and E.S. Wadja, Phys. Rev. 99 (1955) 1085.
[158] D. Wolf, J. Mater. Res. 5 (1990) 1708.
[159] G. Leibfried, Z. Physik 127 (1950) 344.
[160] G.C. Sih and H. Liebowitz, in: Fracture: An Advanced Treatise, ed. H. Liebowitz (Academic Press, New York, 1968).
[161] H. Liebowitz, ed., Fracture, An Advanced Treatise (Academic Press, New York, 1968).